Available online at www.sciencedirect.com
SCIENCE DIRECT®
Precambrian Research 135 (2004) 55–77
Precambrian Research
www.elsevier.com/locate/precamres

Geochemical, $^{40}Ar/^{39}Ar$ geochronological and Sr–Nd isotopic constraints on the origin of Paleoproterozoic mafic dikes from the southern Taihang Mountains and implications for the ca. 1800 Ma event of the North China Craton

Yuejun Wang[a,*], Weiming Fan[a], Yanhua Zhang[b], Feng Guo[a], Hongfu Zhang[c], Touping Peng[a]

[a] *Guangzhou Institute of Geochemistry, Chinese Academy of Sciences, P.O. Box 1131, Guangzhou 510640, China*
[b] *CSIRO Exploration and Mining, P.O. Box 1130, Bentley, WA 6102, Australia*
[c] *Institute of Geology and Geophysics, Chinese Academy of Sciences, Beijing 100029, China*

Received 22 September 2003; accepted 15 July 2004

Abstract

The wide occurrence of Paleoproterozoic mafic dikes in the basement of the Trans-North China Orogen provides important constraints on the major ~1800 Ma tectonothermal event of the North China Craton. These mafic dikes form a tholeiitic series dominated by basalts and basaltic andesites, and can be geochemically classified into three groups: The Groups 1 and 2 rocks are characterized by high total FeO contents (12.69–15.61%), of which the Group 1 rocks are more enriched in LILE and LREE contents and depleted in HFSE ((Th/Nb)*n* = 2.5–3.8, (La/Yb)cn = 3.0–5.8; (Nb/La)*n* = 0.27–0.38) and have more radiogenic Nd isotopic ratios ($\varepsilon_{Nd}(t)$ = −3.40 to −5.14), than the Group 2 rocks ((Th/Nb)*n* = 0.8–1.2, (La/Yb)cn = 1.5–2.1, (Nb/La)*n* = 0.65–0.87, $\varepsilon_{Nd}(t)$ = −0.60 to −1.67). In contrast, the Group 3 rocks are typified by low FeOt (7.86–11.04%) and high MgO (5.62–9.56%) contents. Higher (La/Yb)cn (4.22–7.13) ratios, less radiogenic Nd isotopic ratios ($\varepsilon_{Nd}(t)$ = −2.75 to −5.52), and more significant Th–U and Nb–Ta depletion are also apparent features. $^{40}Ar/^{39}Ar$ geochronology of three representative samples from each group yielded plateau ages of 1780.7 ± 0.5 Ma, 1765.3 ± 1.1 Ma and 1774.7 ± 0.7 Ma, respectively. These elemental and isotopic data suggest that the geochemical variations of these rocks cannot be simply explained by crystallization from a common parental magma involving crustal contamination during emplacement. Instead, they most likely originated from variable sources under different degrees of partial melting. The Group 1 rocks were derived from relatively low degrees of partial melting of a refractory lithospheric mantle previously metasomatised by subduction-related fluids, whereas the Group 2 rocks originated from a hybridized source involving ca. 40% subduction-modified lithospheric mantle, similar to the Group 1, and ca.60%
© 2004 Elsevier B.V. All rights reserved.

* Corresponding author. Tel.: +86 20 85290527; fax: +86 20 85290708.
E-mail addresses: yjwang@gig.ac.cn, wangyj6@21cn.com (Y. Wang).

0301-9268/$ – see front matter © 2004 Elsevier B.V. All rights reserved.
doi:10.1016/j.precamres.2004.07.005

N-MORB component. In contrast, the Group 3 rocks show significant Th–U depletion that may mark the involvement of portions of gabbroic lower crust trapped in the source region during subduction. Based on all the available data, we propose a tectonic model of a full subduction-syncollision-postcollision-rifting cycle for the evolution of the NCC between 1870 and 1765 Ma. A variety of source regions beneath the southern Taihang Mountains initially developed during the period of subduction/collision, and subsequent extension/rifting resulted in the melting of the subduction-modified lithospheric mantle, which produced widespread Paleoproterozoic mafic dikes on the Trans-North China Orogen in response to upwelling of convective mantle.
© 2004 Elsevier B.V. All rights reserved.

Keywords: Geochemistry; $^{40}Ar/^{39}Ar$ geochronology; Paleoproterozoic mafic dikes; ∼1800 Ma event; Southern Taihang Mountains; North China Craton

1. Introduction

The most important tectonothermal event in the North China Craton (NCC) occurred at ∼1800 Ma, and was widely recorded in the early Precambrian rocks (Wu and Zhang, 1998; Zhai, 1999; Zhai and Bian, 2000; Zhai et al., 2001; Zhao, 2001; Zhao et al., 1999, 2000, 2001; Wang et al., 2003a,b; Zhai and Liu, 2003 and references therein). This event has traditionally been named the "Lüliang Movement" and taken to mark the final cratonization of the NCC (Zhao, 1993). However, two different tectonic models have been postulated to account for the ∼1800 Ma event in the NCC. One suggests that the ∼1800 Ma metamorphism and subsequent extension-uplift-magmatism (1800–1650 Ma, Zhang et al., 1994) were caused by a mantle plume related to the break-up of a global pre-Rodinia supercontinent (Zhai and Bian, 2000; Zhai et al., 2001; Zhai and Liu, 2003). The other model suggests a continental collision scenario, proposing that the NCC consists of two Archean blocks (the Eastern and the Western Blocks), separated by the ∼1800 Ma Trans-North China Orogen (also named the Central Zone) shown in Fig. 1a (Zhao et al., 1999, 2000, 2001; Zhao, 2001). This model also proposes that the 1870–1800 Ma metamorphism resulted from the continental–continental collision and that the following period of extension-uplift-magmatism (1800–1650 Ma) was a marker of postcollisional, and intracontinental rifting, reflecting a change of tectonic regime in the NCC (Zhao, 2001; Wang et al., 2003b).

Because of this divergence of views, it is vitally important to characterize the geochemistry of the mafic magmatism that accompanied this event and understand whether it is associated with a mantle plume or subduction/collision. Previous studies have mostly focused on the lithology, geochemistry, geochronology, structure and metamorphic P-T-t path of the metamorphic basement of the NCC (Zhao et al., 1999, 2000, 2001, 2002a,b; Zhao, 2001 and references therein), and little attention has been paid to the mafic dike swarms. There is more than one mafic dike swarm that intruded the basement rocks of the Central Zone (Zhao et al., 2000, 2002; Li et al., 2001), and some earlier ones are metamorphosed. However, there is one mafic dike swarm that is devoid of metamorphism and deformation, and that is one of the most important geological signatures of the ∼1800 Ma event (Qian and Chen, 1987; Halls et al., 2000). This mafic dike swarm should therefore provide important information on mantle processes and the tectonic evolution of the NCC during the Paleoproterozoic. Although preliminary paleomagnetic data, lithochemistry and K–Ar geochronology of these mafic dikes have been reported (Hou and Mo, 1994; Halls et al., 2000; Qian and Chen, 1987; Li et al., 2001), the precise age and systematic geochemistry are rare. Hence, the nature of the mantle source beneath the Central Zone of the NCC at ∼1800 Ma remains poorly constrained.

This study was initiated to conduct systematic geochemical, ^{40}Ar–^{39}Ar geochronological and Sr–Nd isotopic analyses of the unmetamorphosed mafic dikes in the southern Taihang Mountains that may be considered representative of the Proterozoic dike swarm of the Central Zone of the NCC. Our aims are to characterize the nature of the mantle source for the mafic dikes and to advance understanding of the tectonic processes that operated during the ∼1800 Ma event.

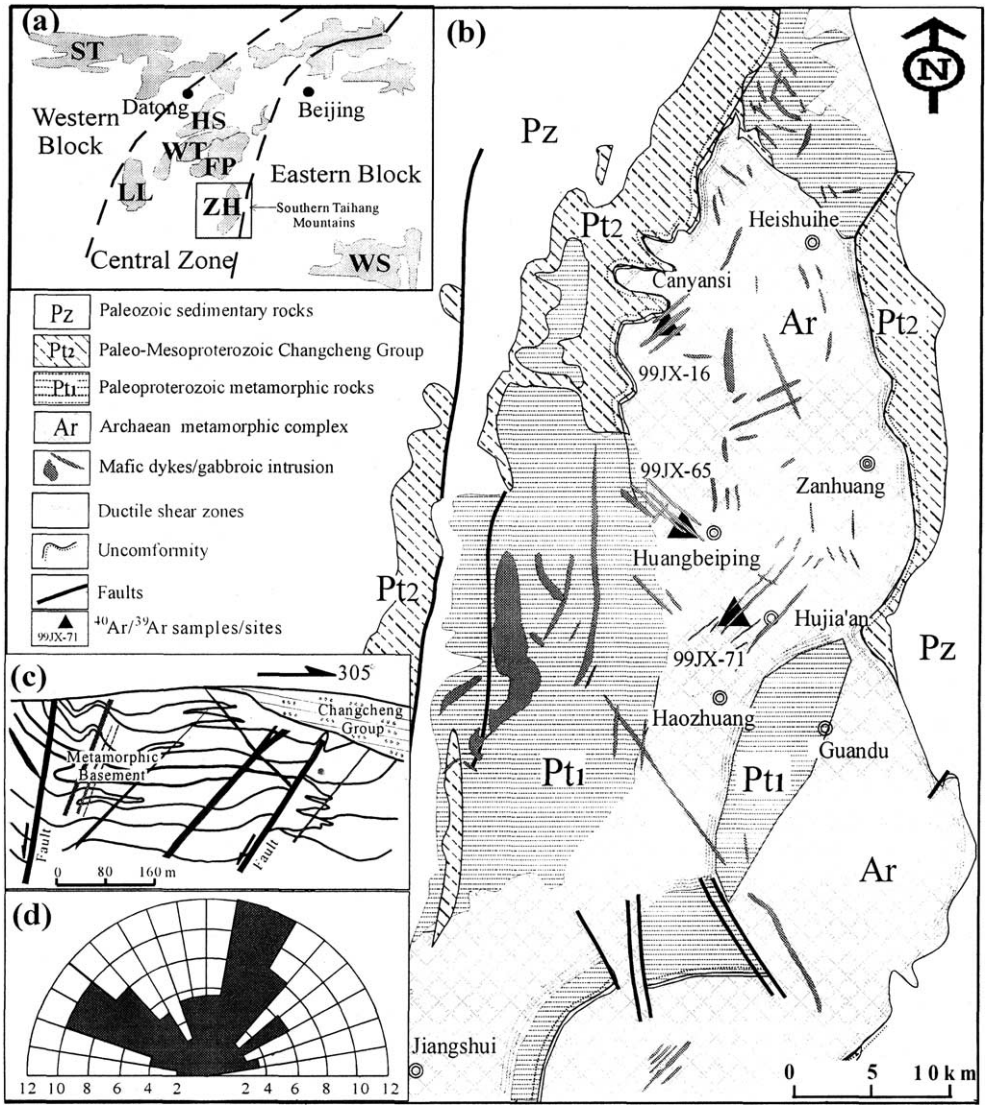

Fig. 1. (a) Schematic map showing major tectonic units of the North China Craton (NCC), and the location of the Zanhuang (ZH), Hengshan (HS), Wutai (WT), Lüliang (LL) and Fuping (FP) domains in the Central Zone of the NCC (after Zhao et al., 1999, 2000). (b) Geological map showing the distribution of the Paleoproterozoic mafic dikes (after Wang et al., 2003a,b, 1997). (c) Geological profile showing how mafic dikes crosscut the metamorphosed basement but subsequently underlie unmetamorphosed Changcheng Group. (d) Rose diagram showing the strike of the dikes in the Zanhuang domain.

2. Geological background and petrology

The North China Craton is one of the ancient cratons in China. It has an ancient crustal basement that is composed of amphibolite to granulite facies Archean grey tonalitic gneisses and greenstones, and Paleoproterozoic khondalites and interlayered clastics (Sun et al., 1992; Liu et al., 2002; Zhao et al., 1999, 2000, 2001; Zhai et al., 2001; Zhai and Liu, 2003). They form a series of mountainous inliers in fault contact with a cover composed of the Mesoproterozoic Changcheng Group and Paleozoic–Mesozoic strata (Halls et al., 2000). Many of the crustal rocks of the NCC were formed at ~2500 Ma, and were affected by the 1870–1800 Ma

tectonothermal event (e.g. Guan et al., 2002; Zhao et al., 2002a,b; Wilde et al., 1997, 1998, 2002; Zhai and Liu, 2003). This event resulted in widespread metamorphism and uplift (Zhao et al., 1999, 2000, 2001, 2002a,b; Wilde et al., 1997, 2002), leading to the final cratonation of the NCC (Zhao et al., 1999).

Proterozoic dike swarms are widespread in the basement of the Central Zone of the NCC, but rare in the Eastern and Western blocks (Qian and Chen, 1987; Zhao et al., 2000). There are two major dike swarms with NWN and WNW trends in the Central Zone, (e.g. in the Hengshan, Wutai, Lüliang, Fuping, Zanhuang domains, see Fig. 1a). The earlier swarm, as in the Hengshan domain, was metamorphosed to amphibolitic and even granulitic facies dikes and retrogressed eclogitic facies that record pressures to 15 kb (Zhao et al., 1999, 2001, 2002a,b; Cooke and O'Brien, 2001). The later mafic dike swarm is commonly devoid of deformation and metamorphism with sporadically chilled margins and baked contacts with country rocks. In general, these unmetamorphosed dikes dip steeply, cut both the Archean and Paleoproterozoic basement, and are covered by Neoproterozoic strata. Earlier K–Ar dating on whole rock samples of these dikes yielded a spectrum of ages between 1.8 and 1.0 Ga (Qian and Chen, 1987; Hou and Mo, 1994). However, Li et al. (2002) reported that metamorphosed mafic dikes from the Hengshan domain were intruded at 2512–2489 Ma (SHRIMP U-Pb zircon) and were overprinted by the ∼1850 Ma tectonothermal event. An unmetamorphosed WNW-striking dolerite dike from the Hengshan domain yielded a single-grain zircon U–Pb age of 1769.1 ± 2.5 Ma, which was interpreted as the intrusive age (Halls et al., 2000; Li et al., 2001). Wang et al. (2003a,b) recently reported the $^{40}Ar/^{39}Ar$ biotite ages of 1820–1790 Ma for the greenschist- to amphibolite-facies gneisses and mylonite, which are interpreted to define the timing of the final regional metamorphism and ductile deformation event. These suggest that the unmetamorphosed/undeformational mafic dikes should be younger than 1790 Ma.

In the southern Taihang Mountains, unmetamorphosed mafic dikes (Fig. 1b) are also widespread. These dikes are typical of those throughout the Central Zone of the NCC, and cut across both the Archean Zanhuang Group and Paleoproterozoic Gangtaohe Group, but are covered by the unmetamorphosed Changcheng Group with an age of <1700 Ma (Wang et al., 2003a,b; Fig. 1c). Many of these dikes follow faults, suggesting syn- or post-faulting emplacement. Based on the measurement of the attitudes of 137 dikes, two average trends of NNE40° and NWN330° are identified (Fig. 1d). The average trend of NNE40° is roughly parallel to the elongation of the Zanhuang metamorphic domain, while the strike of 330° is close to the orientation of the Proterozoic mafic swarms reported from other areas in the NCC. The size of dikes varies widely, with thickness generally ranging from 1 to 30 m (with a maximum of about 100 m), and traceable length ranging from 5 to 20 km (with a maximum of about 50 km). Lithologically, these dikes are dominantly dolerite. Their mineral compositions are plagioclase (25–60% by volume), clinopyroxene (20–50%), biotite (∼2%), amphibole (∼2%), quartz (2–4%), Fe–Ti oxides (1–5%) and minor amounts of euhedral titanite and apatite.

3. Analytical methods

Weathered rims were removed from all rocks. They were then were crushed to millimeter-scale chips for geochemical analyses. Some grains were carefully handpicked under a binocular microscope from separate fractions of selected samples, and only fresh grains of 20–40-mesh size were selected for $^{40}Ar/^{39}Ar$ analyses. The rocks chips for major and trace element and Sr–Nd isotopic analyses were further crushed and powdered to 200-mesh using an agate mill.

Major elements were determined by X-ray fluorescence spectrometry at the Hubei Institute of Geology and Mineral Resource, the Chinese Ministry of Land and Resources. FeO content was analyzed by a wet chemical method. Trace element analysis was performed at the Institute of Geochemistry, the Chinese Academy of Sciences (CAS) with an inductively coupled plasma mass spectrometer (ICP-MS). Detailed sample preparation and analytical procedures follow Qi et al. (2000). The international standard BCR-1 was chosen to calibrate element concentrations of measured samples. Analytical uncertainties were ±1% for major elements and ±5% for most trace elements. The results are presented in Table 1.

The whole rocks samples selected for $^{40}Ar/^{39}Ar$ analyses were individually wrapped in Al-foil packets, encapsulated in sealed Gd-foil, and irradiated in the central thimble position of the nuclear reactor

Table 1
Major and trace element analyses for Paleoproterozoic mafic dikes in the southern Taihang Mountains

Sample	Group 1							Group 2							
	99JX-60	99JX-62	99JX-68	99JX-69	99JX-70	99JX-71	99JX-76	99JX-16	99JX-17	99JX-18	99JX-20	99JX-80	99JX-81	99JX-85	99JX-87
Major oxides (wt.%)															
SiO_2	51.09	50.37	49.23	47.48	47.10	48.06	47.70	49.80	50.00	49.78	50.11	50.67	50.29	50.84	51.01
Al_2O_3	13.40	14.97	13.57	14.04	13.93	13.71	13.76	13.17	13.30	13.29	12.90	13.01	13.04	12.45	12.47
Fe_2O_3	5.13	3.24	4.39	5.36	5.63	4.94	5.70	3.92	3.93	4.11	5.69	4.03	4.07	3.34	4.30
FeO	8.80	9.55	9.37	9.70	9.63	10.43	10.05	8.92	8.73	8.78	7.67	9.73	9.53	11.33	10.60
MgO	5.90	5.57	5.60	6.45	6.40	5.38	5.79	6.34	6.69	6.48	6.14	6.75	6.72	5.66	5.21
CaO	8.49	8.68	9.36	8.41	9.31	8.45	9.28	9.87	9.29	8.96	8.79	9.16	9.26	9.52	9.57
Na_2O	2.48	2.83	2.53	2.68	2.32	2.73	2.64	2.78	2.46	2.90	1.89	2.66	2.71	2.56	2.03
K_2O	0.25	0.46	0.27	0.60	0.49	0.34	0.43	0.62	0.71	0.76	0.98	0.30	0.34	0.35	0.83
MnO	0.18	0.18	0.20	0.21	0.22	0.24	0.24	0.21	0.21	0.20	0.21	0.20	0.21	0.24	0.23
TiO_2	1.24	1.33	1.82	1.29	1.26	1.29	1.31	1.24	1.18	1.21	1.27	1.10	1.08	1.17	1.18
P_2O_5	0.29	0.33	0.32	0.34	0.35	0.33	0.34	0.14	0.13	0.13	0.15	0.11	0.11	0.11	0.11
LOI	2.60	2.47	3.00	3.16	3.10	2.92	2.78	2.82	3.19	3.23	3.98	2.12	2.42	2.26	2.27
Total	99.85	99.98	99.66	99.72	99.74	98.82	100.02	99.83	99.82	99.83	99.78	99.84	99.78	99.83	99.81
$Mg^{\#}$	0.44	0.45	0.43	0.44	0.44	0.39	0.41	0.48	0.50	0.48	0.46	0.48	0.48	0.42	0.39
FeOt	13.42	12.47	13.32	14.52	14.70	14.88	15.18	12.45	12.27	12.48	12.79	13.36	13.19	14.34	14.47
Trace elements															
Sc	37.5	34.2	28.8	35.9	35.9	34.8	39.6	32.3	36.7	38.5	38.5	40.9	40.4	39.9	39.0
V	281	266	275	263	267	276	450	259	277	292	297	350	350	408	403
Cr	141	97	269	187	155	113	113	67	81	82	61.5	119	97	13.7	23.5
Co	51.8	60.3	48.6	77.6	60.5	56.5	68.7	46.3	48.1	51.2	52.7	68.3	65.5	74.6	74.4
Ni	50.2	149	125	139	120	131	123	48.4	54.0	55.3	51.2	81.8	57.6	51.9	50.3
Rb	3.1	8.8	3.4	11.8	9.2	3.3	4.0	21.2	26.5	32.1	36.5	4.0	5.0	2.6	20.5
Sr	165	246	194	193	244	162	203	166	162	174	230	152	178	129	119
Y	38.8	30.4	41.7	28.4	28.6	31.8	26.8	23.4	26.1	27.4	28.1	25.2	24.2	30.2	28.7
Zr	133	129	184	87.7	88.4	111	105	79.2	84.9	95.9	97.7	71.2	76.9	78.4	79.8
Nb	6.41	5.35	9.46	4.92	4.99	5.03	5.03	4.87	5.20	5.73	5.89	5.34	5.82	4.08	3.99
Ba	58.6	114	89.0	436	280	100	227	251	296	278	507	442	564	258	242
La	20.64	15.24	32.13	12.51	13.63	17.61	16.53	6.73	7.39	8.45	8.58	5.94	6.61	7.51	6.90
Ce	44.16	32.75	72.49	29.75	30.46	39.96	36.60	16.41	18.09	20.26	20.63	14.75	15.04	16.45	16.61
Pr	5.51	4.08	9.08	4.00	4.05	5.20	4.96	2.25	2.45	2.69	2.89	2.04	2.09	2.39	2.31
Nd	20.59	18.17	39.71	16.49	17.87	18.38	21.08	10.00	11.01	12.32	12.11	9.88	10.38	10.99	10.36
Sm	5.67	4.84	8.79	4.15	4.28	4.96	5.59	3.09	3.40	3.76	3.46	2.87	3.10	3.00	3.08
Eu	1.45	1.40	2.16	1.20	1.19	1.45	1.52	1.11	1.26	1.39	1.37	0.93	0.92	1.08	1.02
Gd	5.77	4.76	7.59	4.51	4.64	5.13	4.95	3.54	3.90	4.40	4.66	3.38	3.07	3.81	3.71
Tb	0.99	0.85	1.22	0.78	0.82	0.88	0.87	0.66	0.76	0.80	0.82	0.63	0.62	0.73	0.70
Dy	6.32	5.29	7.15	4.79	4.88	5.47	5.14	4.27	4.73	4.93	5.32	4.16	4.12	4.84	4.96
Ho	1.38	1.16	1.56	1.06	1.13	1.20	1.12	0.93	1.09	1.08	1.12	0.90	0.93	1.18	1.15

Table 1 (*Continued*)

Sample	Group 1							Group 2							
Er	4.11	2.95	4.24	2.83	3.07	3.42	3.13	2.50	2.61	2.91	3.24	2.61	2.46	3.30	3.09
Tm	0.60	0.42	0.58	0.43	0.46	0.49	0.49	0.33	0.42	0.41	0.45	0.38	0.36	0.49	0.50
Yb	4.06	2.79	3.95	2.97	2.82	3.39	3.00	2.34	2.82	2.85	2.88	2.68	2.60	3.41	3.32
Lu	0.57	0.37	0.57	0.41	0.46	0.47	0.47	0.36	0.39	0.35	0.39	0.36	0.38	0.49	0.46
Hf	3.54	3.71	5.08	2.21	2.41	2.82	2.81	2.25	2.56	2.95	2.85	1.82	1.92	2.07	2.06
Ta	0.42	0.38	0.62	0.36	0.35	0.29	0.31	0.34	0.34	0.41	0.39	0.33	0.34	0.26	0.25
Pb	4.10	3.84	3.83	3.27	4.49	2.93	3.73	8.48	8.15	8.17	9.78	2.25	2.47	4.88	5.61
Th	2.19	2.39	2.87	1.56	1.59	1.62	1.61	0.53	0.56	0.64	0.62	0.65	0.66	0.67	0.67
U	0.46	0.39	0.43	0.34	0.23	0.28	0.27	0.14	0.17	0.19	0.18	0.18	0.17	0.14	0.13
Th/Ta	5.18	6.29	4.62	4.36	4.50	5.66	5.17	1.58	1.63	1.56	1.60	1.98	1.93	2.61	2.70
$(Nb/La)_N$	0.30	0.34	0.28	0.38	0.35	0.27	0.29	0.70	0.68	0.65	0.66	0.87	0.85	0.65	0.70
$(Th/La)_N$	0.86	1.27	0.72	1.01	0.94	0.74	0.79	0.63	0.61	0.62	0.58	0.88	0.81	0.72	0.79
Ti/Ti*	0.62	0.80	0.70	0.80	0.76	0.71	0.74	0.97	0.83	0.78	0.80	0.90	0.94	0.84	0.88
(La/Yb)cn	3.60	3.87	5.77	2.98	3.42	3.68	3.91	2.03	1.86	2.10	2.11	1.57	1.80	1.56	1.47
(Gd/Yb)cn	1.17	1.41	1.59	1.26	1.36	1.25	1.37	1.25	1.15	1.28	1.34	1.04	0.98	0.93	0.92
Eu/Eu*	0.77	0.90	0.79	0.88	0.90	0.87	0.87	1.02	1.06	1.05	1.05	0.92	0.91	0.98	0.92

	Group 3														
	99JX-01	99JX-02	99JX-03	99JX-04	99JX-05	99JX-06	99JX-07	99JX-08	99JX-49	99JX-51	99JX-54	99JX-56	99JX-57	99JX-58	99JX-65
Major oxides															
SiO_2	50.55	52.63	52.74	52.72	52.30	52.24	52.61	52.85	47.62	49.52	51.24	50.99	50.75	50.54	48.64
Al_2O_3	14.79	14.18	14.23	14.16	14.34	14.41	14.21	14.26	13.72	15.63	14.62	14.76	15.33	15.20	15.18
Fe_2O_3	4.61	4.11	3.71	4.03	4.31	4.62	4.08	4.74	1.49	1.64	1.37	1.08	1.22	1.61	3.86
FeO	6.23	6.73	7.13	6.73	6.60	6.47	6.77	6.02	9.37	6.10	7.78	7.53	7.95	7.72	5.50
MgO	6.13	5.82	5.42	5.47	5.48	5.69	5.53	5.47	11.07	8.14	7.00	8.06	7.19	6.92	7.64
CaO	8.55	7.80	8.56	8.52	8.26	7.78	8.61	8.56	8.66	11.42	9.75	11.15	11.10	10.97	11.34
Na_2O	2.73	2.17	1.75	1.81	1.99	2.14	1.86	1.67	1.55	2.01	2.44	1.82	2.24	2.44	2.90
K_2O	1.10	1.24	1.41	1.39	1.46	1.41	1.31	1.22	1.21	1.54	1.54	1.08	0.75	0.65	0.12
MnO	0.15	0.15	0.16	0.15	0.16	0.17	0.15	0.14	0.18	0.16	0.17	0.16	0.15	0.16	0.16
TiO_2	0.91	1.05	1.06	1.04	1.08	1.07	1.05	1.05	0.71	0.80	0.81	0.67	0.76	0.76	0.65
P_2O_5	0.19	0.23	0.23	0.23	0.24	0.25	0.23	0.23	0.16	0.17	0.18	0.17	0.16	0.16	0.21
LOI	3.85	3.69	3.40	3.53	3.56	3.54	3.35	3.56	4.04	2.66	2.90	2.41	2.20	2.68	3.44
Total	99.79	99.80	99.80	99.78	99.78	99.79	99.76	99.77	99.78	99.79	99.80	99.88	99.80	99.81	99.64
$Mg^{\#}$	0.52	0.50	0.48	0.49	0.48	0.49	0.49	0.49	0.65	0.66	0.58	0.63	0.59	0.58	0.61
FeOt	10.38	10.43	10.47	10.36	10.48	10.63	10.44	10.29	10.71	7.58	9.01	8.50	9.05	9.17	8.97

Table 1 (*Continued*)

	Group 3														
	99JX-01	99JX-02	99JX-03	99JX-04	99JX-05	99JX-06	99JX-07	99JX-08	99JX-49	99JX-51	99JX-54	99JX-56	99JX-57	99JX-58	99JX-65
Trace elements															
Sc	31.7	31.2	30.8	30.8	31.2	30.4	27.0	30.9	23.5	26.5	31.7	30.0	30.1	31.7	33.4
V	222	239	241	240	245	233	215	244	163	184	175	179	211	218	205
Cr	57.7	43.1	42.0	46.0	55.5	71.3	46.4	41.8	754	489	458	421	374	381	303
Co	46.6	45.2	45.0	44.5	44.9	43.2	41.0	44.9	67.2	51.6	38.5	41.5	43.8	42.6	46.7
Ni	80.7	61.2	65.0	62.0	67.7	70.5	58.7	59.4	339	200	119	211	136	130	177
Rb	13.6	16.8	17.6	18.0	20.7	19.9	14.1	15.8	44.9	51.9	41.3	33.1	24.1	20.2	12.6
Sr	318	361	366	360	358	341	328	417	298	388	374	300	397	393	281
Y	20.3	21.1	22.1	21.9	24.1	23.8	19.7	22.6	15.5	17.8	21.4	16.0	18.1	18.4	22.1
Zr	98.1	115	126	130	131	118	111	118	66.4	68.2	77.4	67.5	71.7	68.6	72.8
Nb	3.51	4.39	4.52	4.48	4.67	4.64	3.96	4.57	3.09	3.51	3.98	3.14	3.60	3.56	3.88
Ba	494	499	520	507	514	503	440	461	272	352	398	238	290	239	219
La	14.54	18.31	19.30	18.95	19.71	19.07	16.91	19.35	12.93	14.31	17.72	9.00	11.68	12.31	13.12
Ce	33.78	42.44	43.70	43.32	44.62	43.82	38.32	44.14	29.52	32.54	39.41	21.57	26.41	27.80	28.90
Pr	4.75	5.85	6.04	6.03	6.15	6.16	5.35	5.98	4.03	4.48	4.73	2.87	3.52	3.69	3.76
Nd	19.68	24.49	25.25	24.80	25.82	25.54	22.04	25.04	16.70	18.65	21.16	11.80	15.61	16.18	15.63
Sm	4.27	5.13	5.18	5.26	5.43	5.35	4.53	5.19	3.42	3.89	4.43	3.19	3.88	3.69	3.98
Eu	1.34	1.50	1.56	1.52	1.56	1.56	1.33	1.52	1.10	1.25	1.37	0.97	1.16	1.25	1.20
Gd	4.21	4.67	4.97	4.91	5.13	4.99	4.32	5.01	3.23	3.65	4.53	3.02	3.24	3.39	3.67
Tb	0.65	0.69	0.74	0.74	0.79	0.76	0.63	0.74	0.50	0.56	0.76	0.49	0.56	0.58	0.62
Dy	3.68	3.97	4.05	4.00	4.25	4.23	3.42	4.02	2.79	3.08	3.99	2.92	3.16	3.27	3.92
Ho	0.75	0.77	0.79	0.79	0.84	0.85	0.68	0.79	0.56	0.61	0.85	0.70	0.64	0.70	0.83
Er	2.09	2.12	2.21	2.18	2.33	2.34	1.91	2.18	1.52	1.72	2.14	1.73	1.74	1.79	2.23
Tm	0.31	0.31	0.32	0.32	0.34	0.35	0.28	0.32	0.23	0.26	0.32	0.23	0.23	0.25	0.31
Yb	1.88	1.85	1.98	1.96	2.13	2.14	1.68	1.96	1.39	1.64	1.86	1.51	1.61	1.68	2.13
Lu	0.29	0.28	0.32	0.32	0.33	0.34	0.24	0.29	0.22	0.25	0.27	0.21	0.21	0.23	0.31
Hf	2.34	2.82	3.04	3.10	3.16	3.11	2.41	3.07	1.68	1.79	1.87	1.83	1.98	1.91	1.82
Ta	0.23	0.24	0.25	0.25	0.26	0.26	0.21	0.25	0.20	0.22	0.33	0.22	0.26	0.25	0.27
Pb	3.58	3.79	3.55	3.50	3.56	3.35	3.07	3.61	1.99	2.11	2.29	1.86	1.67	1.80	2.63
Th	0.66	0.71	0.72	0.72	0.80	0.68	0.63	0.78	0.49	0.53	0.65	0.53	0.49	0.44	0.64
U	0.11	0.14	0.14	0.14	0.15	0.13	0.11	0.15	0.10	0.12	0.18	0.12	0.11	0.10	0.16
Th/Ta	2.88	2.91	2.92	2.93	3.09	2.60	3.02	3.19	2.41	2.38	1.95	2.46	1.88	1.79	2.36
$(Nb/La)_N$	0.23	0.23	0.23	0.23	0.23	0.23	0.23	0.23	0.23	0.24	0.22	0.34	0.30	0.28	0.28
$(Th/La)_N$	0.36	0.31	0.30	0.31	0.33	0.29	0.30	0.33	0.31	0.30	0.30	0.48	0.34	0.29	0.40
Ti/Ti*	0.67	0.71	0.67	0.66	0.65	0.66	0.76	0.66	0.68	0.67	0.53	0.66	0.68	0.65	0.53
(La/Yb)cn	5.49	7.02	6.90	6.85	6.55	6.32	7.13	6.99	6.59	6.18	6.73	4.22	4.88	5.21	4.37
(Gd/Yb)cn	1.86	2.09	2.08	2.07	1.99	1.93	2.13	2.12	1.92	1.84	2.01	1.65	1.58	1.67	1.43
Eu/Eu*	0.96	0.92	0.92	0.90	0.89	0.91	0.91	0.90	0.99	1.00	0.93	0.94	0.97	1.06	0.94

FeOt = FeO + 0.9*Fe_2O_3, LOI: Loss on ignition, $Mg^{\#} = Mg^{2+}/(Mg^{2+} + Fe^{2+})$, Eu/Eu* = (Eu)cn/[(Gd)cn + (Sm)cn]/2, Ti/Ti* = $(2*Ti_N/(Gd_N + Tb_N))$. Symbol with "cn" denotes the values normalized to chondrite, and with "$_N$" denotes values normalized against primitive mantle.

Table 2
$^{40}Ar/^{39}Ar$ isotopic analytical data for incremental heating experiments on whole-rock dikes

Temperature (°C)	$(^{40}Ar/^{39}Ar)_m$	$(^{36}Ar/^{39}Ar)_m$	$(^{37}Ar/^{39}Ar)_m$	$(^{38}Ar/^{39}Ar)_m$	$^{39}Ar_k$ (10^{-12} mol)	$(^{40}Ar/^{39}Ar_k)$ ($\pm1\sigma$)	$^{39}Ar_k$ (%)	Apparent age ($t \pm 1\sigma$ Ma)
99JX-16, weight = 0.1712 g								
420	88.09	0.1039	2.0623	0.3442	1.783	57.77 ± 0.034	5.79	970.32 ± 27.46
550	101.47	0.0784	1.6973	0.2892	2.363	78.61 ± 0.029	7.68	1222.64 ± 27.92
670	119.23	0.0659	3.5687	0.3440	2.106	100.3 ± 0.348	6.84	1452.89 ± 36.81
800	142.72	0.0316	2.9849	0.2722	3.658	133.9 ± 0.028	11.80	1758.98 ± 34.45
900	140.57	0.0217	4.2394	0.1975	6.384	134.8 ± 0.020	20.70	1767.19 ± 27.13
1000	144.47	0.0348	4.4079	0.2762	3.978	134.9 ± 0.028	12.90	1767.75 ± 35.03
1100	143.03	0.0303	2.7135	0.2636	3.820	134.5 ± 0.027	12.40	1764.49 ± 33.66
1200	143.11	0.0290	2.8551	0.2739	3.195	135.0 ± 0.028	10.30	1768.66 ± 34.76
1300	148.50	0.0500	2.5670	0.3450	2.315	134.2 ± 0.035	7.52	1761.62 ± 42.28
1450	163.56	0.0990	3.1917	0.5446	1.169	135.0 ± 0.056	3.79	1768.10 ± 64.68
t_p = 1765.3 ± 1.1 Ma, $^{40}Ar/^{36}Ar$ ratio = 286.6, t_t = 1767.4 ± 35.7 Ma, MSWD = 0.52, t_i = 1759.2 ± 2.0 Ma, MSWD = 4.06								
99JX-65, weight = 0.1834 g								
400	255.25	0.1026	4.1900	0.5026	0.902	226.0 ± 0.057	3.29	2405.75 ± 77.51
520	105.12	0.1026	2.6381	0.8846	1.806	75.35 ± 0.0900	6.60	1187.52 ± 79.20
650	126.50	0.0963	4.0105	0.5964	1.920	98.76 ± 0.060	7.01	1439.35 ± 61.45
780	144.89	0.0362	5.3505	0.3442	3.189	135.1 ± 0.035	11.60	1772.04 ± 42.26
900	141.89	0.0243	4.3792	0.1951	5.690	135.3 ± 0.020	20.70	1773.72 ± 27.02
1000	143.73	0.0305	5.8856	0.2691	3.777	135.7 ± 0.027	13.80	1776.95 ± 34.40
1100	142.80	0.0273	5.8864	0.2705	3.373	135.7 ± 0.028	12.30	1777.06 ± 34.52
1200	144.48	0.0330	4.3611	0.2684	3.145	135.4 ± 0.027	11.40	1774.91 ± 34.32
1300	151.30	0.0568	5.1581	0.3784	2.034	135.4 ± 0.039	7.43	1774.80 ± 46.17
1450	152.13	0.0609	4.3362	0.4421	1.517	134.9 ± 0.045	5.54	1770.37 ± 53.07
t_p = 1774.7 ± 0.7 Ma, $^{40}Ar/^{36}Ar$ ratio = 283.9, t_t = 1777.5 ± 24.2 Ma, MSWD = 0.51, t_i = 1769.9 ± 2.0 Ma, MSWD = 0.67								
99JX-71, weight = 0.1786 g								
400	236.52	0.0869	5.4669	0.6196	1.606	212.1 ± 0.0667	3.43	2321.19 ± 88.55
520	72.452	0.0566	1.7986	0.2613	2.456	56.00 ± 0.025	7.94	948.42 ± 21.10
650	109.82	0.0535	1.9320	0.2634	2.594	94.33 ± 0.026	8.39	1393.50 ± 28.28
750	144.75	0.0310	1.8956	0.2586	3.359	135.9 ± 0.026	10.80	1777.79 ± 33.35
850	144.97	0.0301	1.5693	0.2392	4.611	136.3 ± 0.025	14.90	1781.27 ± 31.45
980	143.64	0.0254	1.6971	0.2392	5.909	136.4 ± 0.025	19.10	1781.81 ± 31.41
1100	144.65	0.0290	2.2101	0.2878	3.984	136.4 ± 0.0298	12.80	1782.18 ± 36.40
1200	144.05	0.0297	2.4129	0.2972	3.312	136.2 ± 0.030	10.70	1780.21 ± 37.33
1300	150.24	0.0487	2.5675	0.3346	2.373	136.6 ± 0.034	7.67	1781.01 ± 41.50
1450	168.23	0.1141	3.2957	0.4696	1.256	136.3 ± 0.048	4.06	1780.76 ± 56.77
t_p = 1780.7 ± 0.5 Ma, $^{40}Ar/^{36}Ar$ ratio = 292.7 t_t = 1781.2 ± 17.0 Ma, MSWD = 0.18, t_i = 1778.6 ± 2.0 Ma, MSWD = 2.38								

$\lambda = 5.543e^{-10}/a$, J = 0.01235, $(^{40}Ar/^{39}Ar)_m$: measured values of $^{40}Ar/^{39}Ar$, $^{39}Ar_k$: measured values of $^{39}Ar_k$ which was produced by K decay. t_p, t_t and t_i are plateau age, isochron age and inverse isochron age, respectively.

(1000 kW) at the Chinese Academy of Atomic Energy Science for 2627 minutes with an instantaneous neutron flux of 6.63×10^{12} n/(cm^{-2} s^{-1}). After irradiation, the samples were progressively degassed and purified in steps from 400–420 °C to 1450 °C. Purified argon was finally collected using a Zr–Al getter pump, and subsequently analyzed with a gas source mass-spectrometer operated in the static mode RGA-10 at the Institute of Geology and Geophysics, CAS. The concentrations of ^{36}Ar, ^{37}Ar, ^{38}Ar, ^{39}Ar and ^{40}Ar were corrected for the system blank, radioactive decay of nucleogenic isotopes, and minor interference reactions involving Ca, K and Cl. The details of the analytical and correction techniques can be found in Sang et al. (1996). An internal standard amphibole (BSP-1) was used as a monitor, the age of which is 2060 ± 18.6 Ma. The results of $^{40}Ar/^{39}Ar$ thermochronology analyses are listed in Table 2.

Table 3
Sr–Nd isotopic analyses for Paleoproterozoic mafic dikes in the southern Taihang Mountains

Sample	Sm	Nd	Rb	Sr	$^{147}Sm/^{144}Nd$	$^{87}Rb/^{86}Sr$	$^{143}Nd/^{144}Nd$ (2σ)	$^{87}Sr/^{86}Sr$ (2σ)	$^{87}Sr/^{86}Sr(t)$	$\varepsilon_{Nd}(t)$
Group 1										
99JX-62	4.84	18.17	5.78	246.0	0.161	0.068	0.511985 (11)	0.706232 (17)	0.704527	−4.75
99JX-69	4.15	16.49	11.76	193.0	0.152	0.177	0.511954 (6)	0.709722 (17)	0.705278	−3.40
99JX-70	4.28	17.87	9.17	244.1	0.145	0.109	0.511797 (10)	0.707769 (13)	0.705028	−4.79
99JX-76	5.59	21.08	3.99	203.2	0.160	0.057	0.511956 (8)	0.706528 (14)	0.705094	−5.14
Group 2										
99JX-16	3.09	10.00	15.21	166.3	0.187	0.265	0.512436 (10)	0.712056 (14)	0.705388	−1.67
99JX-18	3.76	12.32	22.07	174.1	0.184	0.368	0.512414 (9)	0.714497 (15)	0.705248	−1.62
99JX-20	3.46	12.11	30.47	229.6	0.173	0.385	0.512292 (10)	0.714934 (17)	0.705254	−1.45
99JX-81	3.10	10.38	4.98	178.4	0.181	0.081	0.512422 (11)	0.706673 (17)	0.704635	−0.60
99JX-87	3.08	10.36	20.46	119.0	0.180	0.499	0.512385 (10)	0.717161 (17)	0.704618	−1.17
Group 3										
99JX-02	5.13	24.49	6.75	361.2	0.127	0.054	0.511668 (8)	0.705326 (16)	0.704022	−3.23
99JX-04	5.26	24.80	8.00	359.8	0.128	0.064	0.511643 (8)	0.705783 (11)	0.704248	−4.07
99JX-07	4.53	22.04	4.08	327.8	0.124	0.036	0.511665 (8)	0.704993 (16)	0.704112	−2.75
99JX-54	4.43	21.16	31.35	373.7	0.127	0.243	0.511664(11)	0.711091 (9)	0.704989	−3.32
99JX-56	2.87	11.80	33.13	300.0	0.147	0.320	0.511785 (9)	0.712802 (13)	0.704747	−5.52
99JX-58	3.69	16.18	10.19	392.9	0.138	0.075	0.511703 (9)	0.706326 (13)	0.704445	−5.06

Sr and Nd isotopic ratios were measured by MC-ICP-MS at the Guangzhou Institute of Geochemistry, CAS. The analytical procedures for Sr–Nd analyses are the same as reported by Wei et al., 2002 and Liang et al., 2003. The $^{87}Sr/^{86}Sr$ ratio of the NBS 987 standard and $^{143}Nd/^{144}Nd$ ratio of the La Jolla standard were 0.710265 ± 12 and 0.511862 ± 10, respectively. The measured $^{87}Sr/^{86}Sr$ and $^{143}Nd/^{144}Nd$ ratios were normalized to $^{86}Sr/^{88}Sr$ = 0.1194 and $^{146}Nd/^{144}Nd$ = 0.7219, respectively. $^{87}Rb/^{86}Sr$ and $^{147}Sm/^{144}Nd$ ratios were calculated using the Rb, Sr, Sm and Nd abundances measured by ICP-MS. The measured and age-corrected $^{87}Sr/^{86}Sr$ and $\varepsilon_{Nd}(t)$ are listed in Table 3.

4. Results

4.1. Geochemical characteristics

4.1.1. Classification of mafic dikes

The mafic dikes can be divided into three main types (Groups 1, 2 and 3) based on variations in FeOt (FeOt = FeO + 0.9*Fe_2O_3) content, and their distinctive (Nb/La)*n* and (Th/Nb)*n* ratios. The Groups 1 and 2 rocks have high FeOt of 12.69–15.61%, while the Group 3 rocks have low FeOt (7.86–11.04%). Group 1 has (Nb/La)*n* = 0.27–0.38 and (Th/Nb)*n* = 2.6–3.8, whereas Group 2 has (Nb/La)*n* = 0.65–0.87 and (Th/Nb)*n* = 0.8–1.2. Fig. 2a illustrates the differences in FeOt content and (Nb/La)*n* ratio of these groups. When plotted on the Nb/Y versus SiO_2 diagram (Winchester and Floyd, 1977), all these rocks belong to the subalkaline series and are composed of basalt and basaltic andesite (Fig. 2b). Similar results can be obtained in the TAS diagram (LeBas et al., 1986; not shown). Using the classification of Jensen (1976), the Groups 1 and 2 samples plot in the high-Fe tholeiitic basalt field of the tholeiitic series, but the Group 3 rocks plot close to the high-Mg tholeiitic basalt field (Fig. 2c).

4.1.2. Major oxides and compatible elements

The Groups 1 and 2 rocks both display small variations in major oxide contents (Fig. 3), with SiO_2 = 48.71–52.53% (volatile-free), MgO = 5.34–6.92%, FeOt = 12.69–15.61%, TiO_2 = 1.11–1.48%, mg-number = 0.39–0.50, Cr = 14–269 ppm, and Ni = 48–149 ppm. There are compositional differences between the Groups 1 and 2 rocks, with the former showing higher Al_2O_3, FeOt, TiO_2 and P_2O_5, and lower SiO_2 and CaO than the latter (Table 1). The Group 3 rocks have a much wider range with SiO_2 = 48.74–54.93%, MgO = 5.62–9.56%, FeOt = 7.86–11.04%, TiO_2 = 0.68–1.12%, Cr = 42–754 ppm, and Ni = 59–339 ppm. The mg-numbers are in the range of 0.48–0.68. In general, the Groups 1 and 2 rocks ex-

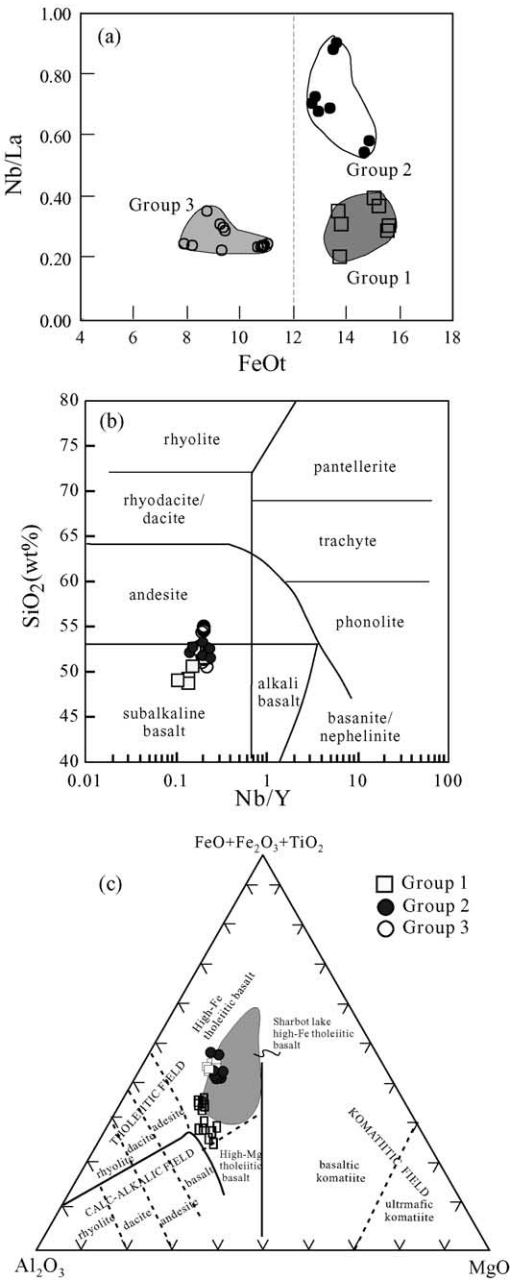

Fig. 2. (a) Nb/La vs. FeOt (=FeO + 0.9*Fe_2O_3), (b) SiO_2 vs. Nb/Y, and (c) FeO + Fe_2O_3 + TiO_2 – Al_2O_3 – MgO diagrams. (b) and (c) are after Winchester and Floyd (1977) and Jensen (1976), respectively.

hibit lower SiO_2, Al_2O_3, Ni and Cr contents, but higher FeOt, TiO_2 V and Sc contents than Group 3 rocks with comparable MgO values (Table 1 and Fig. 3). For the Group 3 rocks, MgO correlates negatively with SiO_2, FeOt, P_2O_5 and TiO_2, but positively with Al_2O_3, CaO, Ni, Cr and CaO/Al_2O_3 (Fig. 3). In contrast, for the Groups 1 and 2 rocks, there is only a positive correlation of Al_2O_3 and Cr with MgO; other oxides are relatively constant, irrespective of MgO content (Fig. 3).

4.1.3. Incompatible elements

The incompatible element compositions exhibit distinct variations between the groups (Table 1). The Group 1 rocks have weakly negative Eu anomalies with Eu/Eu* = 0.77–0.90, whereas the Group 2 rocks have Eu/Eu* values of 0.91–1.06. The Group 1 rocks show slight REE fractionation with (La/Yb)cn = 2.98–5.77 and (Gd/Yb)cn = 1.17–1.59, but the Group 2 rocks show a flat REE pattern ((La/Yb)cn = 1.47–2.11 and (Gd/Yb)cn = 0.92–1.34). In contrast to both these groups, the Group 3 rocks have (La/Yb)cn = 4.22–7.13 and (Gd/Yb)cn = 1.43–2.13, showing strong REE fractionation, with Eu/Eu* = 0.89–1.06 (Table 1). In the primitive-mantle normalized spidergrams (Fig. 4), the Group 1 rocks are characterized by marked Nb–Ta, Sr and Ti, and slight Zr–Hf negative anomalies. In contrast, weak Th–U, Nb–Ta, and P–Ti negative anomalies are present in the Group 2 rocks. The Group 3 rocks display significant Th–U, Nb–Ta, P–Ti, and slight Zr–Hf negative anomalies. We also noted that Groups 1 and 2 rocks show the differences in the degree of light rare earth element (LREE) enrichment and the magnitude of Nb–Ta–Ti and Th–U anomalies. For example, the Groups 1 and 3 rocks exhibit significant depletion of Nb relative to La, with (Nb/La)n = 0.22–0.38, in clear contrast to Group 2 rocks where (Nb/La)n = 0.65–0.87 (Fig. 2a and Table 1). There is also more significant depletion of Th and U relative to La in the Group 3 rocks, with (Th/La)n = 0.29–0.48, compared with that of other groups where (Th/La)n = 0.72–1.27 for Group 1, and 0.58–0.88 for Group 2.

4.2. $^{40}Ar/^{39}Ar$ geochronology

Representative whole-rock samples for $^{40}Ar/^{39}Ar$ analyses were collected from the centers of three fine-grained dolerite dikes (10–15 m in width) from Hujia'an, Zanhuang (JX-71 of Group 1), Canyansi,

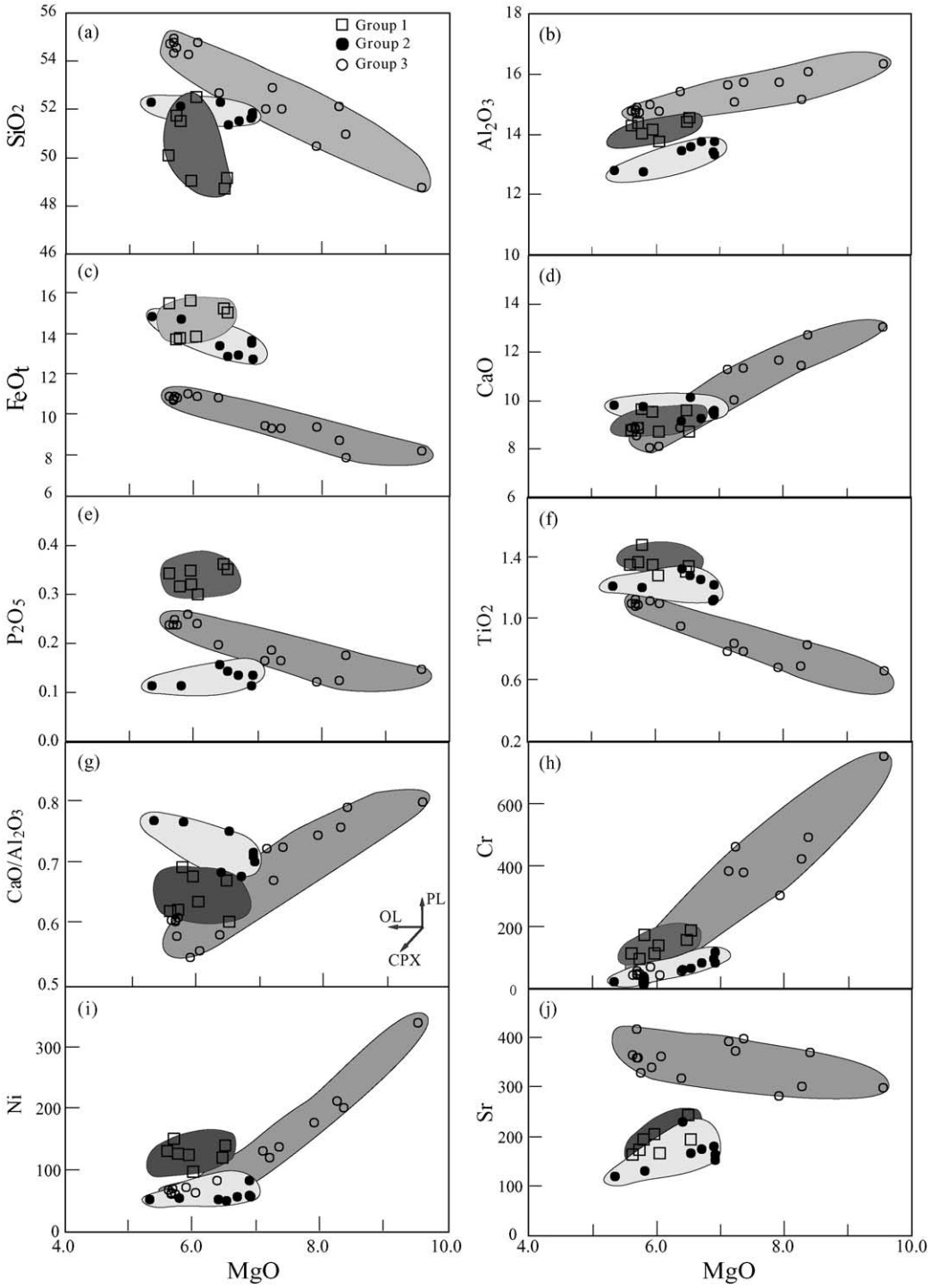

Fig. 3. Variation diagrams of (a) SiO_2, (b) Al_2O_3, (c) FeOt (=FeO + 0.9*Fe_2O_3), (d) CaO, (e) P_2O_5, (f) TiO_2, (g) CaO/Al_2O_3, (h) Cr, (i) Ni and (j) Sr vs. MgO for Paleoproterozoic mafic dikes in the Zanhuang domain. All major oxides are normalized to 100% on a volatile-free basis.

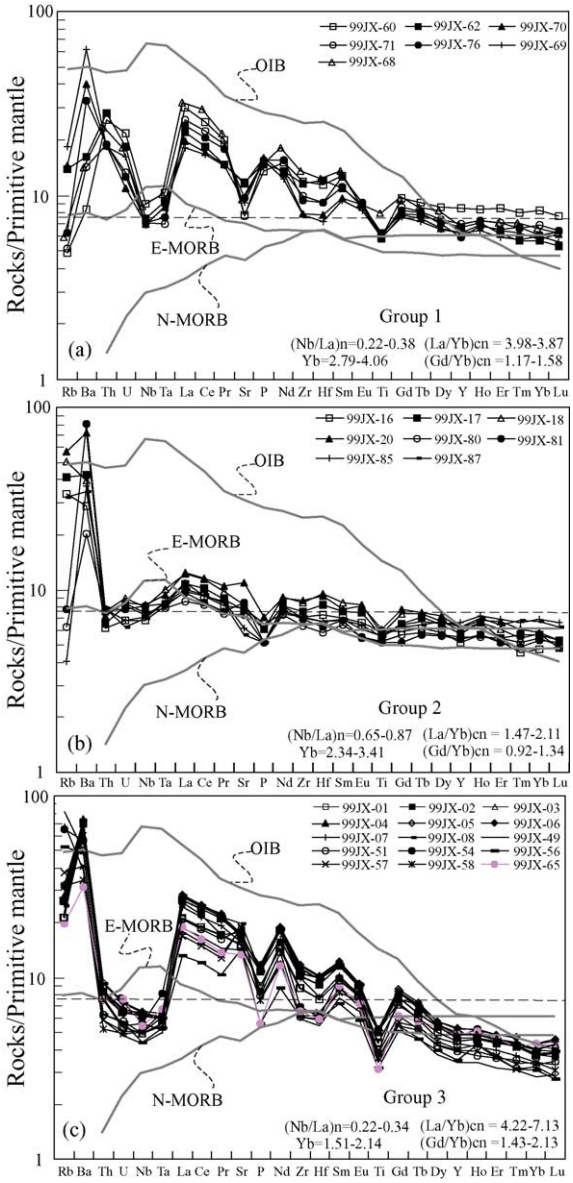

Fig. 4. Primitive mantle-normalized trace element patterns for unmetamorphosed Paleoproterozoic mafic dikes in the Zanhuang domain. (a): Group 1; (b): Group 2; (c): Group 3. Normalizing values, and OIB, N-MORB and E-MORB fields are from Sun and Mcdonough (1989). (Nb/La)*n* value is normalized against primitive mantle, and (La/Yb)cn and (Gd/Yb)cn are normalized to chondrite.

Jingxing (JX-16 for Group 2), and Huangbeiping, Zanhuang (JX-65 from Group 3), respectively (Fig. 1b). The trends of the three dikes are NE48° (JX-71), NW340° (JX-65) and NE40° (JX-16), respectively.

All the three samples have $^{40}Ar/^{39}Ar$ spectra with similar characteristics (Fig. 5a, c and e), and yielded plateau ages of 1780.7 ± 0.5 Ma (99JX-71), 1765.3 ± 1.1 Ma (99JX-16) and 1774.7 ± 0.7 Ma (99JX-65), which are defined by 80–83% of total ^{39}Ar released for seven successive intermediate- and high-temperature steps at 1σ level of uncertainty. Their Ca/K ratios ($Ca/K = 1.78{*}^{37}Ar_{Ca}/^{39}Ar_K$) show little variation with successive heating steps. Their isochron- and inverse isochron-ages (Fig. 5b, d and f) are similar to the plateau ages (Table 2), and the inverse ordinate intercepts ($^{40}Ar/^{36}Ar$ ratios = 283.9–292.7) yielded by the $^{36}Ar/^{40}Ar-^{39}Ar/^{40}Ar$ data are slightly lower than the $^{40}Ar/^{36}Ar$ ratio of 295.5 in the present-day atmosphere (Table 2), suggesting no significant excess ^{40}Ar or ^{36}Ar loss. Therefore, the plateau ages (1765–1781 Ma) are deemed to be reliable.

The approximate timing of mafic dike intrusion can also be defined from several data sources. A pegmatite vein from the Fuping complex, which offsets the regionally metamorphosed and deformational structures dated at 1875–1802 Ma (Zhao et al., 2002a,b), yielded a zircon SHRIMP U–Pb age of 1790 ± 8 Ma (Wang et al., 1997; Wilde et al., 1998). The Zanhuang complex has striking similarities in lithology, time of major magmatism, deformation and metamorphic history to the Fuping complex (Zhao et al., 2002a,b; Liu et al., 2002; Wang et al., 2003a). The last regional ductile deformational structures in the Zanhuang complex were dated at 1820–1790 Ma (mineral $^{40}Ar/^{39}Ar$ method, Wang et al., 2003a,b). The other constraint is that the oldest age for the unmetamorphosed Changcheng Group is considered to be ~1700 Ma (Lu and Li, 1991; Wang et al., 2003b). All these facts suggest that the undeformed and unmetamorphosed mafic dikes were very likely intruded during the time interval of 1790–1700 Ma. This is supported by the single-grain zircon U–Pb age of 1769.1 ± 2.5 Ma reported for the unmetamorphosed WNW-striking dolerite dike from the Hengshan domain (Halls et al., 2000). Therefore, the plateau ages of 1781–1765 Ma from the current study can be interpreted to date the intrusion of these mafic dikes.

4.3. Sr–Nd isotopes

The mafic dike rocks have a very narrow range in Sr isotopic ratios ($^{87}Sr/^{86}Sr(t)$ = 0.704022–0.705388),

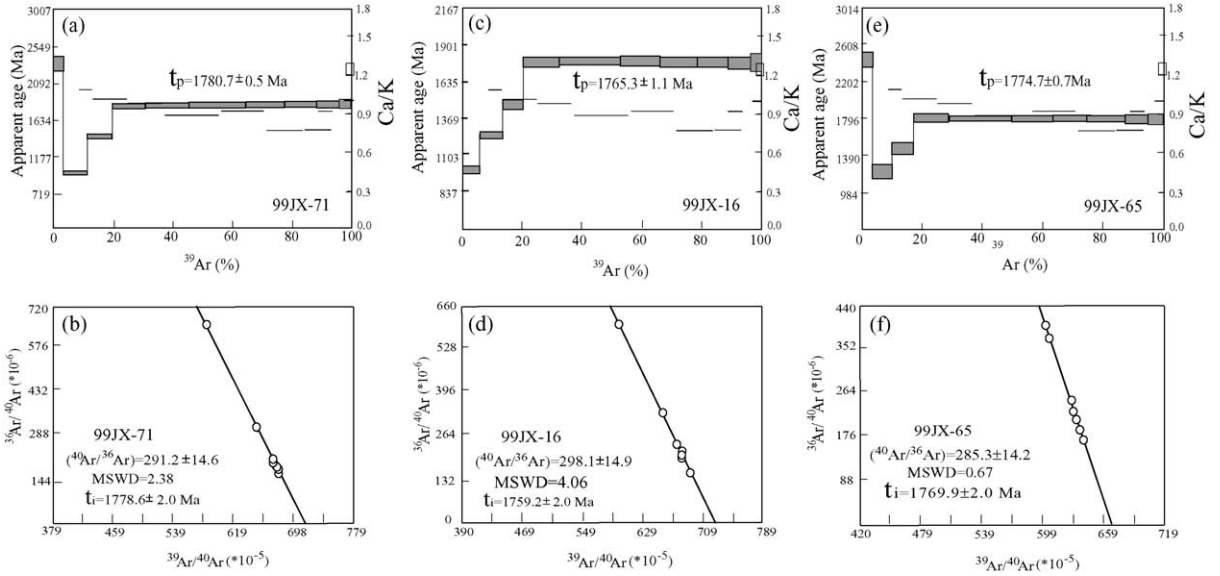

Fig. 5. $^{40}Ar/^{39}Ar$ age spectra and Ca/K ratios (a): 99JX-71, (c): 99JX-65, (e): 99JX-16, and inverse isochron age (b): 99JX-71, (d): 99JX-65, (f): 99JX-16 of three mafic dikes from the Zanhuang domain. Broad lines give the apparent ages (the width of the bars reflects 1σ uncertainty), and fine lines show Ca/K ratios. See Fig. 1b for the location of the samples.

and variable Nd isotopic values ($\varepsilon_{Nd}(t)$ = −0.60 to −5.52), similar to that of the rift-related Paleoproterozoic Xiong'er volcanics in the NCC ($\varepsilon_{Nd}(t)$ = −3.8 to −9.0, Zhao et al., 2002a,b). In the $^{87}Sr/^{86}Sr(t)$ versus $\varepsilon_{Nd}(t)$ diagram (Fig. 6), most of the samples plot into the field with $\varepsilon_{Nd}(t)$ value of less than 0 and $^{87}Sr/^{86}Sr(t)$ ratio of >0.7045. The Group 1 rocks have $\varepsilon_{Nd}(t)$ = −3.40 to −5.14, similar to that of Group 3 (−2.75 to −5.52). However, the Group 2 rocks show relatively higher $\varepsilon_{Nd}(t)$ values (−0.60 to −1.67).

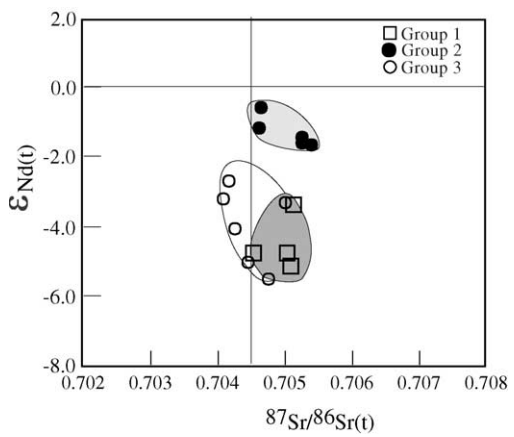

Fig. 6. $\varepsilon_{Nd}(t)$ (t = 1770 Ma) vs. initial $^{87}Sr/^{86}Sr(t)$ diagram for Paleoproterozoic mafic dikes in the Zanhuang domain.

5. Discussion

The compositional variations amongst the three groups identified in the preceding sections most likely reflect complicated magmatic processes and/or the nature of the source. These characteristics can generally be attributed to: (1) various amounts of assimilation-fractional crystallization of mantle-derived magma and crustal contamination en route; (2) various degrees of partial melting of a homogeneous source at different pressures and temperatures; and (3) mantle source variability, e.g. metasomatised lithospheric mantle or hybridized source (Bell and Simonetti, 1996).

5.1. Alteration effects

The mafic dikes in the region might have been altered to various degrees after intrusion, which can be determined from petrographic observations and relatively high loss on ignition in almost all the samples (2.20–4.01%). Some incompatible elements, such as

Rb, Ba and K, are known to be mobile during weathering (Deniel, 1998), as demonstrated by the considerable scatter in primitive–mantle-normalized patterns shown in Fig. 4. The age-correction of measured $^{87}Sr/^{86}Sr$ involves Rb concentrations, and thus the effect on initial $^{87}Sr/^{86}Sr$ ratios is particularly important. However, the consistency demonstrated by the data set (except for Rb, K and Ba) in primitive–mantle-normalized patterns (Fig. 4), suggests that absolute abundances and ratios of incompatible elements, such as REE, Th, U, Nb, Ta, Zr, Hf, Y, Ti, are the least sensitive to weathering. This is supported by a large number of studies (Jochum et al., 1991; Deniel, 1998; Kerrich et al., 1999; Xu et al., 2001). Accordingly, the following discussions focus on these immobile elements and $\varepsilon_{Nd}(t)$ value.

5.2. Crustal contamination and magma fractionation

The Group 1 rocks have high Th content and Th/Ta ratios of 3.84–6.29 (Table 1), but relatively constant (Nb/La)*n*, $^{87}Sr/^{86}Sr(t)$ ratios and $_{Nd}(t)$ values irrespective of SiO_2 content (Tables 1 and 3). This suggests that these rocks encountered little to no crustal contamination during their ascent. The Group 2 and 3 rocks contain low Th and U contents, with Th/Ta ratios (1.56–3.19) near that of primitive mantle values (2.3). Although (Nb/La)*n* ratios for the Group 2 rocks tend to decrease with magma evolution (Table 1), there is no trend of increasing $^{87}Sr/^{86}Sr(t)$ ratios or decreasing $\varepsilon_{Nd}(t)$ values with increasing SiO_2, as would be expected in rocks affected by crustal contamination. The (Nb/La)*n* ratios of 0.22–0.38 (average 0.31) for the Group 1 and 3 rocks are near or even lower than that of the average crust. The broad similarity in immobile incompatible element behavior for each group also suggests negligible crustal contamination en route through the crust. High (Nb/La)*n* ratios (0.65–0.87) for Group 2 therefore may reflect the source characteristics rather than crustal contamination.

Most mafic dikes do not represent primary melts, as judged from their low MgO (mostly <8.0%), $Mg^{\#}$ (0.39–0.68) and Ni contents (48–339 ppm). These characteristics suggest that they underwent a degree of fractional crystallization in magma chambers prior to emplacement. The Group 3 rocks may have experienced fractionation of olivine and clinopyroxene from the parental magmas, supported by the positive correlation between MgO and Cr and Ni (Fig. 3h and i). The decrease of CaO/Al_2O_3 with lowering MgO indicates clinopyroxene fractionation (Fig. 3g). It is also noted that Sr content increases slightly as MgO decreases (Fig. 3j) and there are negligible negative Eu anomalies, indicating that fractionation of plagioclase might be insignificant.

Although the details of the fractionation of the Groups 1 and 2 dikes are less well constrained, due to the narrow compositional range, clinopyroxene fractionation for Group 1 and olivine fractionation for Group 2 can be proposed, based on the low $Mg^{\#}$ values, and Cr and Ni contents (Fig. 3h and i). Plagioclase fractionation is essential for the Group 1 rocks, as reflected in negative Sr anomalies (Fig. 4a) and low Eu/Eu* values of 0.77–0.90. However, distinct incompatible element ratios and $\varepsilon_{Nd}(t)$ values (Tables 1 and 3) suggest that these geochemical features can not be explained by a simple fractionation relationship amongst the groups. It is more likely that they have evolved from different parental magmas.

5.3. Degree of partial melting

The distinct incompatible element patterns between the groups might be related to various degrees of partial melting or to different depths of melting. In general, low La/Yb ratios reflect a melting regime dominated by relatively large melt fractions and/or spinel as the predominant residual phase, whereas high La/Yb ratios are indicative of smaller melt fractions and/or garnet control (Xu et al., 2001; Deniel, 1998). Therefore, the high (La/Yb)*n* and (Gd/Yb)*n* ratios, in combination with relatively low HREE abundance, for the Group 3 rocks suggest that they may have formed by low degrees of partial melting of a garnet-bearing source. The relatively low P_2O_5/Al_2O_3 ratios (0.008–0.017) for these rocks also indicate a relatively low percentage of melting. For the Group 2 rocks, the flat REE patterns, near-chondritic (Gd/Yb)*n*, and low total REEs, but relatively high HREE and Y abundances, suggest a relatively high percentage of melting of mantle sources in the absence of garnet. The Group 1 rocks exhibit similar fractionation of HREE, but their relatively higher (La/Yb)*n* ratios in comparison with the Group 2 rocks indicate that their formation involved a lower degree of melting. The sample 99JX-68 has a higher (La/Yb) ratio and concentration of incompatible elements than the oth-

ers, being likely ascribed to a lower degree of partial melting.

The question remains as to whether these dikes possibly represent the products of proportional partial melting of a similar source. However, the ratios of incompatible elements with similar distribution coefficients (e.g. Th/Nb, Zr/Nb, Nb/La), which are the least susceptible to partial melting and fractional crystallization processes, show regular variation amongst the groups as illustrated in Table 1. Such variations in incompatible element ratios and isotopic compositions potentially argue against a scenario that they were generated by variable degrees of partial melting of the same homogeneous source. We believe, therefore, that these differences most likely reflect source variability (i.e. two or more source components were involved).

5.4. Source characteristics

The Group 1 and 3 rocks show negative Nb–Ta anomalies and low ε_{Nd} (t) values, and the former also have high Th–U contents (Figs. 4a and c). These fingerprints indicate that a crustal component must have been involved in the generation of these mafic dikes. The most likely source therefore is the continental lithospheric mantle due to negligible crustal contamination during ascent, as discussed above.

Depletion of Ta relative to La generally results from metasomatism of the mantle source by subduction-related processes, and low (Hf/Sm)n ratios imply a mantle source that underwent carbonatitic metasomatism (LaFlèche et al., 1998). The relatively high (Hf/Sm)n and low (Ta/La)n ratios of the Group 1 and 3 rocks indicate that the cause of metasomatism may be a subduction- rather than a carbonatite-related process (Fig. 7a). Nb is depleted relative to the LREEs and negative Nb–Ta and Zr–Hf anomalies are well defined in the Group 1 and 3 rocks. These characteristics, together with low $\varepsilon_{Nd}(t)$ values and relatively high LILE/HREE (or LILE/HFSE) ratios, are commonly interpreted as the signatures of the addition of subduction-related fluids into a depleted mantle source (Kepezhinskas et al., 1997). The trends in Fig. 7b and c are also consistent with an increase in hydrous metasomatism in their mantle source. Therefore, the Group 1 rocks most likely originated from a lithospheric mantle metasomatised by subducted fluids. In the diagrams of the incompatible element ratios (Fig. 8a–c), Groups 1, 2 and 3 rocks exhibit two distinct linear trends. One formed by the Group 1 and Group 2 rocks strongly suggest the mixing of the subduction-related lithospheric mantle end member characterized by the Group 1 rocks and MORB-like component end member. The other constituted by the Group 3 rocks implies mixing of the subduction-related lithospheric mantle, characterized by the Group 1 rocks, and the lower crust end member with higher La/Nb and Zr/Nb, but lower Y/Nb, Th and U contents (Figs. 8a–c). Same conclusion is also observed in the plot of incompatible elemental versus isotopic ratio (Fig. 8d).

Th–U depletion can be partially caused by plagioclase accumulation in gabbros with extremely low (Th, U)/Pb ratios (Gancarz and Wasserburg, 1977; Sobolev et al., 2000) and low partition coefficients for Th and U relative to Ba and La (LaTourette et al., 1995). This is also supported, to some extent, by the extremely low (Th/La)n ratio of 0.02 ± 0.01 for gabbros from Samail (Chen and Pallister, 1981) and the Precambrian Gabal Gerf ophiolite in Egypt (Zimmer et al., 1995). Therefore, significant Th–U depletion in Figs. 4 and 7d suggests the possibility that the Group 3 rocks were the product of a refractory metasomatised lithospheric mantle mixed with a gabbroic component. Then the question arises whether the involvement of gabbros occurred in the source region or en route through the crust. A possible scenario is that metasomatised lithospheric mantle-derived magmas rose through the crust–mantle boundary and mixed with gabbro-derived melts (Xu et al., 2001). Assuming that the Group 1 rocks represent the metasomatised lithospheric end-member component and that (Th/La)n is stable during the partial melting and crystallized fractionation, modeling calculations show that, to obtain the low (Th/La)n ratios of 0.29–0.48 (average of 0.34) for the Group 3 rocks, at least 65% gabbro-derived melts are required (even with the assumption of extremely low (Th/La)n of 0.01 for gabbro-derived melts). It is unlikely that such a high percentage of gabbro-derived melts was involved in the formation of the Group 3 rocks. The other possible scenario is that the large negative Th–U anomalies resulted from the involvement of recycled plagioclase-rich gabbros in the magma source (Hofmann and Jochum, 1996; Sobolev et al., 2000). In general, oceanic gabbros have high Nb/La ratios and $\varepsilon_{Nd}(t)$ values, and are likely to have substantial positive Sr and smaller positive Eu anomalies (Hofmann and Jochum, 1996; Sobolev et

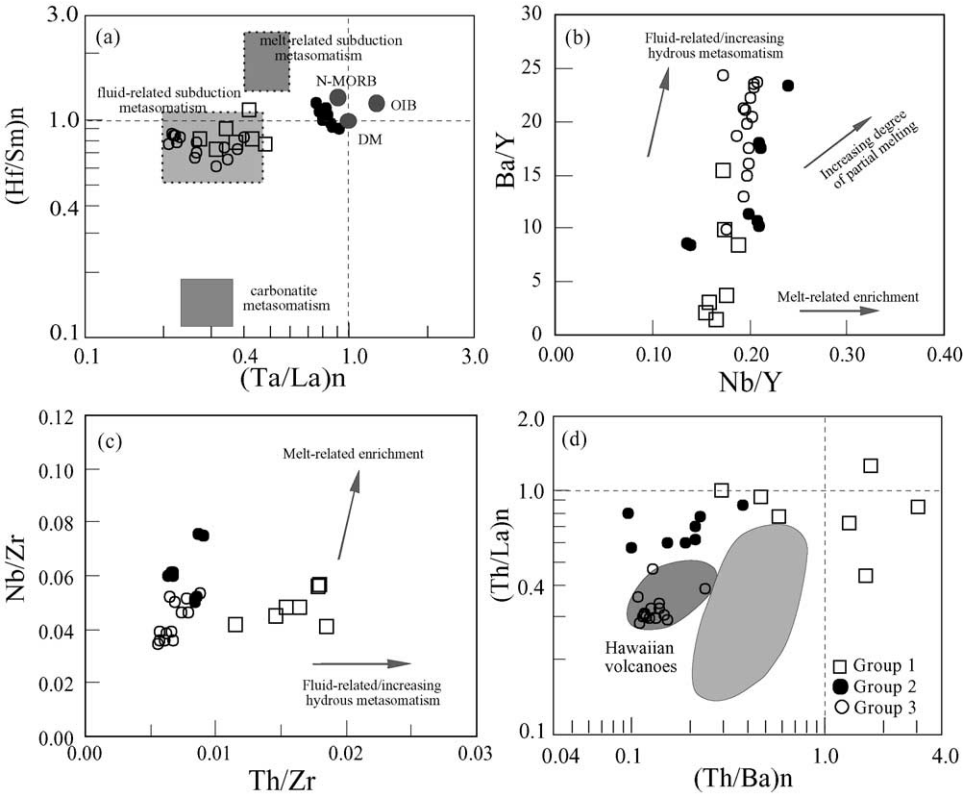

Fig. 7. Plots of (a) (Hf/Sm)*n* vs. (Ta/La)*n*, (b) Ba/Y vs. Nb/Y, (c) Nb/Zr vs. Th/Zr, and (d) (Th/Ba)*n* vs. (Th/La)*n* for Paleoproterozoic mafic dikes in the Zanhuang domain. (a) and (b) are respectively after Hofmann and Jochum (1996) and LaFlèche et al. (1998) while (c) and (d) are from Kepezhinskas et al. (1997). The correlation in (c) and (d) suggests that the source of these mafic dikes has undergone fluid-related rather than melt-related subduction metasomatism. The low Th basalts from Hawaiian volcanoes (Hofmann and Jochum, 1996) are shown as shaded fields in (d).

al., 2000). However, except for a slightly positive Sr anomaly in a few samples (99JX-51, -56, -57), insignificant Sr and Eu anomalies for most Group 3 rocks do not support the involvement of recycled oceanic gabbros. As shown in Figs. 7 and 8, the gabbroic end-member is required to have lower Nb/La, Y/Nb and Th–U, more indicative of a gabbroic contribution from the lower crust (Hemond et al., 1994). We here propose that the Group 3 rocks were derived from a hybridized source involving subduction-related lithospheric mantle and recycled gabbroic material. The gabbroic relics in the lower crust likely came from rocks similar to either the high-pressure Jinggangku Formation (dominantly gabbro/diorite) within the Wutai sequence (Zhao et al., 1999) or earlier mafic dikes. In the Wutai/Hengshan area (Fig. 1a) the gabbroic component, which was possibly deformed to reach eclogite facies (Cooke and O'Brien, 2001) during subduction, was recycled into the mantle as eclogitic layers or pods to hybridise with refractory peridotites (Hemond et al., 1994), and such a scenario is proposed were for the Taihang Mountains.

As illustrated in Fig. 8, the Groups 1 and 2 rocks plot along an array distinct from that of the Group 3 rocks, and can be interpreted in terms of mixing between an end-member with the characteristics of Group 1 and an end-member component with low Zr/Nb but high Nb/La and $\varepsilon_{Nd}(t)$ values, possibly equivalent to N-MORB. A positive correlation between Zr/Nb and Y/Nb for Groups 1 and 2 (Fig. 8a) clearly indicates mixture of N-MORB with Group 1 end-member. High (Th/La)*n* and (Ta/La)*n* ratios, and (Hf/Sm)*n* ratios near that for the N-MORB end member (Fig. 7a and b),

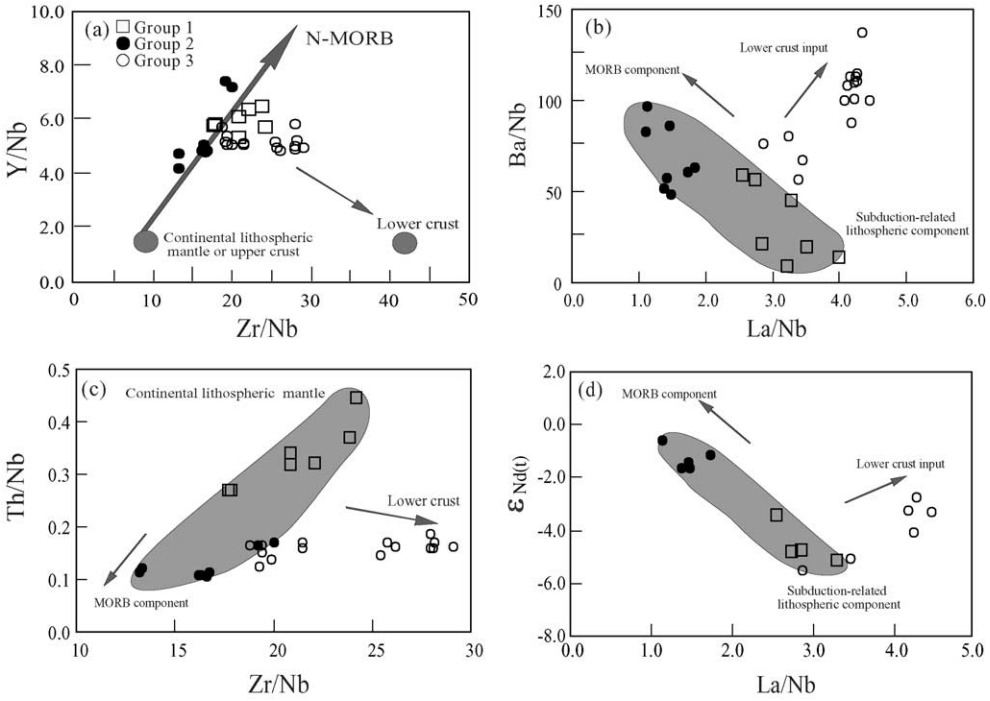

Fig. 8. Plots of (a) Y/Nb vs. Zr/Nb; (b) Ba/Nb vs. La/Nb; (c) Th/Nb vs. Zr/Nb; and (d) $\varepsilon_{Nd}(t)$ vs. La/Nb for Paleoproterozoic mafic dikes in the Zanhuang domain. Also shown are the average compositions for the upper and lower crust (Taylor and McLennan, 1985), and N-MORB (Sun and Mcdonough, 1989). The data for the Groups 1 and 2 rocks follow a mixing array represented by the N-MORB and subduction-modified continental lithospheric mantle end members. The data of the Group 3 rocks define another mixing array characterized by subduction-modified lithospheric mantle and lower crustal end-members.

also suggest participation of an N-MORB component in the generation of Group 2. To quantitatively determine the respective contributions of the two end-members, modeling of incompatible element ratios has been performed using Group 1 and N-MORB as two potential components. The results (Fig. 9) show that the addition of about 60% N-MORB component into a subduction-modified lithospheric mantle can account for the variations of the incompatible element ratios in the Group 2 rocks. When the calculation parameters of Nd (ppm) and $\varepsilon_{Nd}(t)$ are 12 and −5 for the subduction-related lithospheric end-member, and 7 and +6 for the N-MORB end-member, respectively (Sun and McDonough, 1989; Hawkesworth et al., 1984), a similar proportion of N-MORB component (50–60%) can explain the Nd isotopic variations. Consequently, we explain the isotopic and incompatible elemental characteristics of the Group 2 rocks as resulting from a high degree of partial melting of a mixture between N-MORB mantle and a subduction-modified lithospheric mantle.

We also need to address the important issue concerning the iron-enrichment in the Groups 1 and 2 rocks. The Groups 1 and 2 rocks with high total FeO (FeOt) contents have higher Ti/Ti* (0.62–0.97, average of 0.80) than the “normal” Group 3 rocks (0.53–0.76, average of 0.66, Table 1). This is inconsistent with the fact that high-FeOt liquids should evolve at a relatively lower oxidation state than common tholeiitic magma (Juster and Grove, 1989), indicating that the high FeOt of the Groups 1 and 2 rocks might not be the result of low-pressure fractionation of a primitive magma with normal iron contents (Hanski, 1992). Experimental data show that FeOt in primitive magmas is positively related to pressure and, at a given pressure, the FeOt in melts increases with increasing degrees of partial melting (Hirose and Kushiro, 1993). Following this reasoning, the high FeOt of the Groups 1 and 2

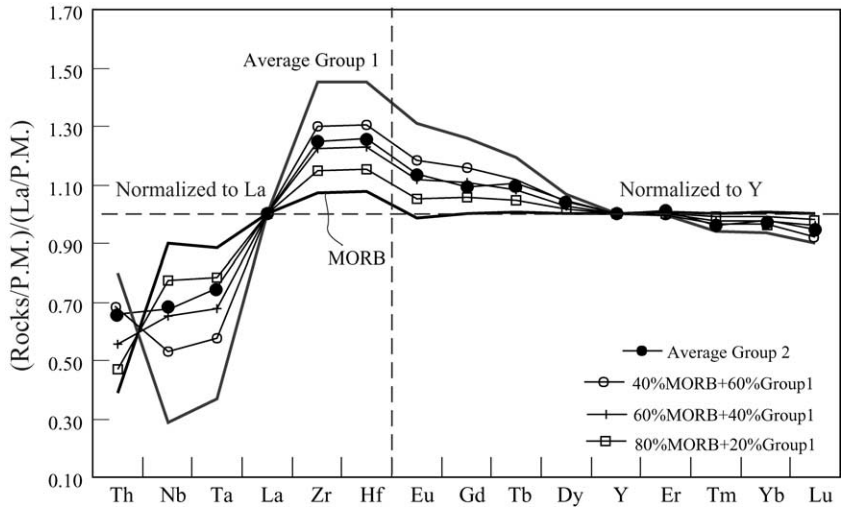

Fig. 9. Modeling of the incompatible element ratios using the Group 1 rocks and N-MORB as two potential components. Strongly (from Th to Hf) and moderately (from Eu to Lu) incompatible elements are normalized to La and Y, respectively. Addition of ca.60% N-MORB component into the lithospheric mantle can account for the variations of the incompatible element ratios for the Group 2 magmas.

rocks was probably generated at a higher pressure than Group 3, and the Group 2 rocks (with higher degrees of partial melting) should have higher FeOt than the Group 1 rocks. This is in fact contrary to the results discussed above. Hence, different pressure conditions and/or various degrees of partial melting cannot adequately explain the high-FeOt contents of the Groups 1 and 2 rocks. A more reasonable explanation is that the high FeOt contents in the magmas were inherited from the source.

Although there is no direct modern analogy to explain the petrogenesis of high FeOt rocks (Leybourne et al., 1999) due to their unique chemistries, four speculative possibilities have been suggested to account for the iron-rich nature of the source. These are: (1) Fe-rich streaks in mantle plume starting-heads (Herzberg and Zhang, 1996; Gibson et al., 2000; Kerrich et al., 1999); (2) "normal" lherzolite with eclogite/pyroxenite blobs/streaks (Hauri, 1996; Takahasi et al., 1998); (3) mantle wedge metasomatised by slab melt and/or delaminated refractory slab (Leybourne et al., 1999); and (4) garnet-free refractory mantle residue (Hanski and Smolkin, 1995). However, as discussed above, the dikes dominantly occur in the Central Zone of the NCC, and only rarely in the Eastern and Western blocks. The Group 1 rocks with high FeOt contents exhibit the fingerprint of a subduction-modified lithospheric component. The Group 2 rocks (with lower FeOt than Group 1) likely had a high proportion of N-MORB involvement. These characteristics appear to preclude the possibility of streaks in mantle plume starting-heads as the Fe-rich source. The Groups 1 and 2 rocks display higher FeOt contents than the Group 3 rocks, which are interpreted as the product of lithospheric mantle hybridized by a gabbroic (possible eclogitic) component. This indicates that the involvement of eclogite/pyroxenite blobs can probably be ruled out in the generation of high-FeOt magma in the region. Therefore, it is speculated that generation of these high FeOt rocks is most likely related to partial melting of a garnet-free refractory mantle residue (Hanski and Smolkin, 1995). The refractory mantle residues may have relatively high FeOt contents, and this will increase during melting, due to the moderately incompatible affinity of FeOt (Hirose and Kushiro, 1993). The gabbroic input would probably lower the FeOt of the Group 3 magma (Xu et al., 2001).

5.5. Tectonic implications

As discussed previously, there are two distinct models for the ~1800 Ma tectonothermal event in the Central Zone of the NCC. One proposes rifting related to mantle plumes (Zhai and Liu, 2003), and the other to

a continental collision (Zhao et al., 1999, 2000, 2001; Zhao, 2001). Our data for the Paleoproterozoic mafic dikes provide some important constraints on this debate and the evolution of the NCC.

The three groups of mafic dikes have different origins. Group 1 was derived from refractory lithospheric mantle metasomatised by subduction-related fluids, Group 2 originated from a mixture of refractory metasomatised lithospheric mantle with a proportion of an N-MORB component; and Group 3 was the product of a hybridized source between subduction-related lithospheric mantle and a substantial amount of gabbroic component trapped into the source region during subduction. These results appear to support the fact that the source of these mafic rocks was initially related to subduction-collision processes rather than to a mantle plume.

Information from SHRIMP U–Pb dating indicates that only one generation of metamorphic zircons occurs in the metamorphic complexes in the Central Zone of the NCC, which were dated at 1870–1820 Ma (e.g. Wang et al., 1997; Wu and Zhang, 1998; Guan et al., 2002; Zhao et al., 2000, 2001, 2002a,b; Zhao, 2001). Wang et al. (2003a) considered that D_2 deformation in the region was dominated by WNW-ESE shortening and top-to-ESE thrusting in a collisional environment. The D_3 event (1820–1790 Ma) was characterized by divergent extensional (Zhang et al., 1994) and ductile shearing as a result of post-collision extensional collapse and exhumation of the thickened crust (Wang et al., 2003a). The D_1–D_2–D_3 sequence dated at 1870–1790 Ma seems to represent a full collision-thrusting/thickening-extensional collapse cycle. These data provide important support for the suggestion that the Central zone of the NCC resulted from subduction-collision between the Western and Eastern Blocks at 1870–1820 Ma (Zhao et al., 1999, 2000, 2001, 2002a,b; Zhao, 2001).

The formation of these mafic dikes (1781–1765 Ma) post-dated the D_3 post-collisional extension (1820–1790 Ma). In Zr–Zr/Y and Ti–Ti/Zr diagrams (Fig. 10), all samples plot within, or near to, the within-plate basalt field. This indicates that these mafic dikes might have been generated during intracontinental rifting as evidenced by the contemporaneous Miaoxiangshan- Miyun and Zhongtiaoshan-Xiong'er rifting-type magmatism in the NCC at ~1760 Ma (Zhao et al., 2002a,b). Due to the high density of

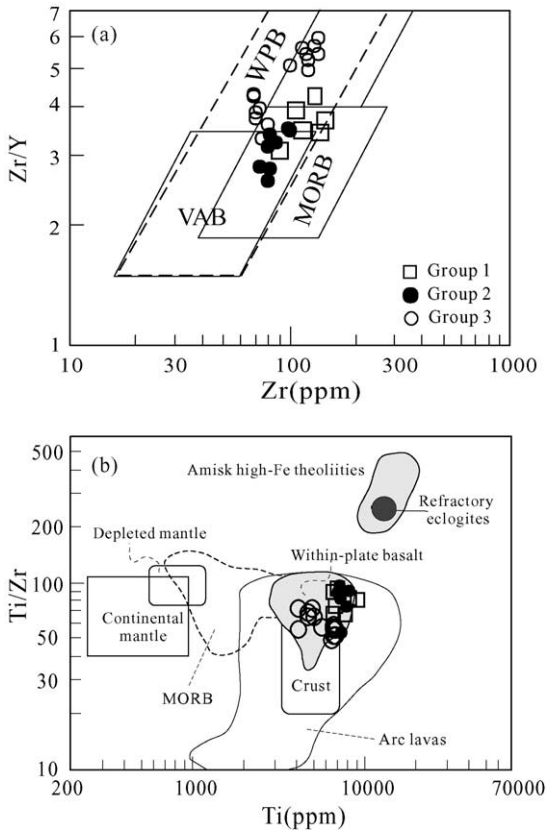

Fig. 10. Geochemical discrimination diagrams for Paleoproterozoic mafic dikes in the Zanhuang domain; (a) Zr/Y vs. Zr is after Pearce and Norry (1979), and (b) Ti/Zr vs. Ti is after Leybourne et al. (1999).

the iron-rich magma (2.78–2.83 g/cm^3), the upward transport of large amounts of melt would be difficult. Brooks et al. (1991) suggested that only part of such a magma could rise to reach the surface/subsurface when rapid rifting or extension occurred. The Groups 1 and 2 rocks have higher FeOt contents in comparison to normal tholeiitic basalts, highlighting the importance of the rifting/extension environment. This is also supported by reports that Fe-rich magma/basaltic glasses are commonly observed at divergent plate margins (Brooks et al., 1991).

Taking into account the geochemical characteristics and the $^{40}Ar/^{39}Ar$ geochronology, we propose here that a variety of source regions of the Paleoproterozoic mafic dikes initially developed during the period of Paleoproterozoic subduction/collision between the Eastern and Western blocks of the NCC,

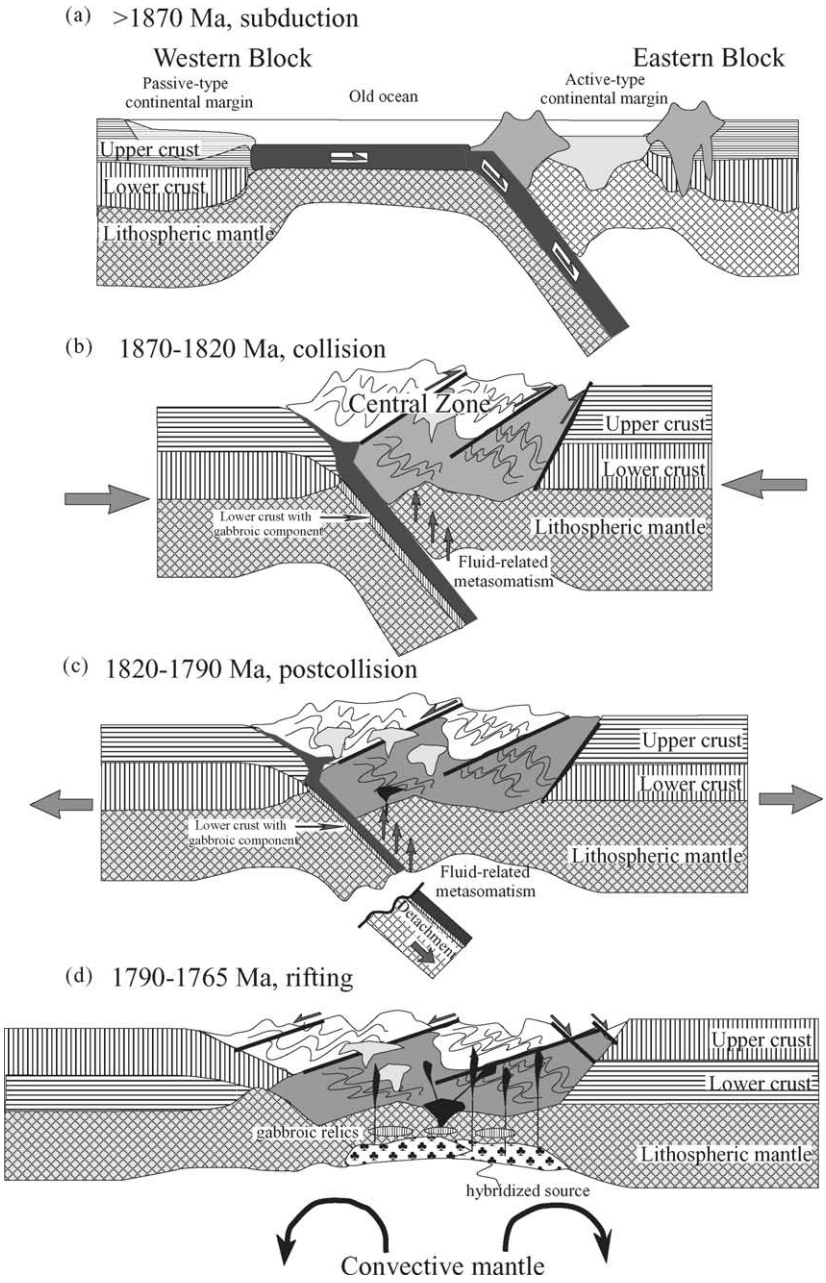

Fig. 11. Schematic cartoons showing a full subduction-collision-postcollision-extensional rifting cycle in the NCC between 1870 and 1760 Ma; (a) >1870 Ma: the Western Block was subducted beneath the Eastern Block; (b) 1870–1820 Ma: Collision between the Western and Eastern Blocks, resulting in crustal thickening and subduction-related modification of lithospheric mantle, and accompanied by the production of a variety of source regions; (c) 1820–1790 Ma: postcollision collapse resulting in extensional deformation and slab detachment; (d) 1790–1765 Ma: rifting associated with upwelling of convective mantle, inducing the generation of Paleoproterozoic mafic magma in the southern Taihang Mountains.

and subsequently extension led to the formation of actual magma in response to the uprising of asthenospheric mantle. Ascending convective mantle heated overlying garnet-free refractory mantle residue that was previously metasomatised by a subduction-related fluid. This resulted in the formation of the Group 1 magma with island-arc geochemical affinity. Almost simultaneously, a mixed source of metasomatised refractory mantle, with some proportion of gabbroic lower crust that was trapped into the source region during subduction, was also partially melted to produce the Group 3 rocks. The progressive upwelling of convective mantle not only supplies heat, but also causes thermo-mechanical erosion of subduction-modified lithospheric mantle. As a result, a thermo-mechanically eroded refractory lithospheric mantle was gradually intermingled into upwelling N-MORB-like convective mantle near the base of the lithospheric mantle (Chung et al., 1994; Gorring et al., 2003). The hybridized source was subsequently melted to generate Group 2 magma.

Incorporating the data from previous studies (Zhao et al., 1999, 2000, 2001, 2002a,b; Zhao, 2001; Wang et al., 2003a and references therein), Fig. 11 summarizes a tectonic scenario for the full subduction-syncollision-postcollisional-rifting cycle in the temporal evolution of the NCC between ca.1870 Ma and 1765 Ma. Before 1870 Ma, the Western Block was subducted beneath the Eastern Block along the Central Zone (Fig. 11a), with a component gabbroic lower crust subducted to mantle depths. During the syncollisional stage (1870–1820 Ma), sedimentary rocks of the Western Block were thrust over the Eastern Block. This caused crustal-scale folding, thrusting and metamorphism. This tectonic process was also accompanied by the development of subduction-modified lithospheric mantle (Fig. 11b). Between 1820 and 1790 Ma, the orogenic belt (the Central Zone) underwent post-collision extensional collapse. This was marked by exhumation of thickened crust, retro-metamorphism, kilometer-scale uplifting and possibly slab detachment (Fig. 11c). Rifting then developed between 1790 and 1765 Ma due to thermal-mechanical erosion of the lithospheric mantle in response to upwelling of convective mantle, resulting in magma generation of these mafic dikes in the Central Zone of the NCC (Fig. 11d). The geochemical differences between the three groups were the result of various degrees of melting of heterogeneous sources formed during previous subduction/collision.

Acknowledgements

The authors would like to thank S.A. Wilde and M. Sun for their thorough, critical and constructive reviews and comments, and A. Kröner for his helpful editorial advise. We also thank Y.G. Xu for helpful discussions and suggestions, and W.L. Kuang and C.L Liao for their help during fieldwork. Financial support for this study was jointly provided by China Natural Science Foundation (40303005, 49973021) and Chinese Academy of Science (KZCX1-107, GIGCX-03-01) Grants.

References

Bell, K., Simonetti, A., 1996. Carbonatite magmatism and plume activity: implications from the Nd, Pb isotope systematics of Oldoinyo Lengai. J. Petrol. 37, 1321–1339.

Brooks, C.K., Larsen, L.M., Nielsen, T.F.D., 1991. Importance of iron-rich tholeiitic magmas at divergent plate margins: a reappraisel. Geology 19, 269–272.

Chen, J.H., Pallister, J.S., 1981. Lead isotopic studies of the Samail ophiolite, Oman. J. Geophys. Res. 86, 2699–2708.

Chung, S.L., Sun, S.S., Tu, K., Chen, C.H., Lee, C.Y., 1994. Late Cenozoic basaltic volcanism around the Taiwan Strait, SE China: product of lithosphere–asthenosphere interaction during continental extension. Chem. Geol. 112, 1–20.

Cooke, R.A., O'Brien, P.J., 2001. Resolving the relationship between high P-T rocks and gneisses in collisional terrane: an example from the Gföhl gneiss-granulite association in the Moldanubian Zone, Austria. Lithosphere 58, 33–54.

Deniel, C., 1998. Geochemical and isotopic (Sr, Nd, Pb) evidence for plume-lithosphere interactions in the genesis of Grande Comore magmas (Indian Ocean). Chem. Geol. 144, 281–303.

Gancarz, A.J., Wasserburg, G.J., 1977. Initial Pb of the Amitsoq genesis. Geochim. Cosmachim. Acta 41, 1283–1301.

Gibson, S.A., Thompson, R.N., Dickin, A.P., 2000. Ferropicrites: geochemical evidence for Fe-rich streaks in upwelling mantle plumes. Earth Planet. Sci. Lett. 174, 355–374.

Gilder, S.A., Keller, G.R., 1991. Eastern Asian and the western Pacific: timing and spatial distribution of rifting in China. Tectonophysics 197, 225–243.

Gorring, M., Singer, B., Growers, J., Kay, S.M., 2003. Plio-Pleistocene basalts from the Meseta del Lago Buenos Aires, Argentina: evidence for asthenosphere-lithosphere interactions during slab window magmatism. Chem. Geol. 193, 215–235.

Guan, H., Sun, M., Wilde, S.A., Zhou, X.H., Zhai, M.G., 2002. SHRIMP U–Pb zircon geochronology of the Fuping Complex: implications for formation and assembly of the North China Craton. Precamb. Res. 113, 1–18.

Halls, H.C., Li, J.H., Davis, D., Hou, G.T., 2000. A precisely dating Proterozoic palaeomagnetic pole from the North China craton and its relevance to palaeocontinental reconstruction. Geophys. J. Int'l. 143, 185–203.

Hanski, E.J., 1992. Petrology of the Pechenga ferropicrites and cogenetic, Ni-bearing gabbro-wehrlite intrusions, Kola Peninsula, Russia. Geol. Surv. Finland, Bull. 367, 192.

Hanski, E.J., Smolkin, V.F., 1995. Iron- and LREE-enriched mantle source for early Proterozoic intraplate magmatism as exemplified by the Pechenga ferropicrites, Kola Peninsula Russia. Lithos 34, 107–125.

Hauri, E.H., 1996. Major-element variability in the Hawaiian mantle plume. Nature 382, 415–419.

Hawkesworth, C.J., Rogers, N.W., van Calsteren, P.W.C., Menzies, M.A., 1984. Mantle enrichment processes. Nature 311 (27), 331–335.

Hemond, C., Devey, C.W., Chauvel, C., 1994. Source compositions and melting processes in the Society and Austral plumes (South Pacific Ocean): element and isotope (Sr, Nd, Pb, Th) geochemistry. Chem. Geol. 115, 7–45.

Herzberg, C., Zhang, J.Z., 1996. Melting experiments on anhydrous peridotite KLB-1: compositions of magmas in the upper mantle and transition zone. J. Geophys. Res. 101, 8271–8295.

Hirose, K., Kushiro, I., 1993. Partial melting of dry peridotites at high pressures: Determination of compositions of melts segregated from peridotite using aggregates of diamond. Earth Planet. Sci. Lett. 114, 477–489.

Hofmann, A.W., Jochum, K.P., 1996. Source characteristics derived from very incompatible trace elements in Mauna Loa and Mauna Kea basalts, Hawaii Scientific Drilling Project. J. Geophys. Res. 101 (B5), 11831–11839.

Hou, G.T., Mo, Z.G., 1994. K–Ar ages and their geological significance of late Precambrian mafic dike swarms emplacement in North China Craton. J. Mineral Geol. North China 9 (3), 267–270 (in Chinese).

Jensen, L.S., 1976. A new cation plot for classifying subalkaline volcanic rocks. Ont. Geol. Survey, Miscellaneous, 66.

Jochum, K.P., Arndt, P.N.T., Hofmann, A.W., 1991. Nb–Ta-La in komatiites and basalts: constraints on komatiite petrogenesis and mantle evolution. Earth Planet. Sci. Lett. 107, 272–289.

Juster, T.C., Grove, T.L., 1989. Experimental constraints on the generation of Fe–Ti basalts, andesites and rhyodacites at the Galapagos Spreading Center, 85 °W and 95 °W. J. Geophys. Res. 94 (B7), 9251–9274.

Kepezhinskas, P., McDermott, F., Defant, M.J., Hochstaedter, A., Drummond, M.S., 1997. Trace element and Sr–Nd–Pb isotopic constraints on a three-component model of Kamchatka Arc petrogenesis. Geochim. Cosmochim. Acta 61 (3), 577–600.

Kerrich, R., Polat, A., Wyman, D., Hollings, P., 1999. Trace element systematics of Mg- to Fe-tholeiitic basalt suites of the Superior Province: implications for Archean mantle reservoirs and greenstone belt genesis. Lithos 46, 163–187.

LaFlèche, M.R., Camiré, G., Jenner, G.A., 1998. Geochemistry of post-Acadian, Carboniferous continental intraplate basalts from the Maritimes basin, Magdalen islands, Québec, Canada. Chem. Geol. 148, 115–136.

LaTourette, T., Hervig, R.L., Holloway, J.R., 1995. Trace element partitioning between amphibole, phlogopite and basanite melt. Earth Planet. Sci. Lett. 135, 13–30.

LeBas, M.J., LeMaitre, R.W., Streckeisen, A., Zanettin, B., 1986. A chemical classification of volcanic rocks based on the total alkali-SiO_2 diagram. J. Petrol. 27, 745–750.

Leybourne, M., Wangoner, N.V., Ayres, L., 1999. Partial melting of a refractory subducted slab in a Paleoproterozoic island arc: implications for global chemical cycles. Geology 27 (8), 731–734.

Li, J.H., Hou, G.T., Qian, X.L., 2001. The single-grained zircon U–Pb dating of Hengshan Mesoproterozoic mafic dike swarm and its implication for tectonic evolution, North China Craton. Geol. Rev. 47 (3), 234–238 (in Chinese with English abstract).

Li, J.H., Kröner, A., Huang, X.N., 2002. The discovery of the Neoarchean mafic dike swarm in Hengshan and reinterpretation of the previous "Wutai greenstone belt". Science in China (series D). 45 (8), 680–690.

Liang, X.R., Wei, G.J., Li, X.H., Liu, Y., 2003. Precise measurement of $^{143}Nd/^{144}Nd$ and Sm/Nd ratios using multiple-collectors inductively couple plasma-mass spectrometer (MC-ICP-MS). Geochimica 32 (1), 91–96.

Liu, S.W., Pan, Y.M., Li, J.H., Li, Q.G., Zhang, J., 2002. Geological and isotopic geochemical constraints on the evolution of the Fuping Complex, North China Craton. Precamb. Res. 117, 41–56.

Lu, S.N., Li, H.M., 1991. U-Pb dating of single grain zircon of volcanic rocks from Dahongyu Formation in the Changcheng Group, jixian. Bull. Chin. Acad. Geol. Sci. 5, 111–114.

Pearce, J.A., Norry, M.J., 1979. Petrologenetic implications of Ti, Zr, Y and Nb variations in volcanic rocks. Contrib. Mineral. Petrol. 69, 33–47.

Qi, L., Hu, J., Greggoire, C., 2000. Determination of trace elements in granites by inductively coupled plasma mass spectrometry. Talanta 51, 507–513.

Qian, X.L., Chen, Y.P., et al., 1987. Late Precambrian mafic swarms of the North China Craton. In: Halls, H.C. (Ed.), Mafic Dike Swarms Geol. Assoc. Can. Spec. Papers, 34, pp. 385–391.

Sang, H.Q., Wang, S.S., Qiu, J., 1996. The ^{40}Ar-^{39}Ar ages of pyroxene, hornblende and plagioclase in Taipingzhai granulites in Qianxi County, Hebei Province and their geological implications. Acta Petrol. Sinica 12 (4), 390–400 (in Chinese with English abstract).

Sobolev, A.V., Hofmann, A.W., Nikogosian, I.K., 2000. Recycled oceanic crust observed in 'ghost plagioclase' within the source of Mauna Loa Lavas. Nature 404 (27), 986–990.

Sun, M., Armstrong, R.L., Lambert, R.J., 1992. Petrochemistry and Sr, Nd, Pb isotopic geochemistry of early Precambrian rocks, Wutaishan and Taihangshan areas, China. Precamb. Res. 56, 1–31.

Sun, S.S., Mcdonough, W.F., 1989. Chemical and isotopic systematic of ocean basalt: implications for mantle composition and processes. In: Saunders, A.D., Norry, M.J. (Eds.), Magmatism in the Ocean Basin, 42. Geol. Soc. Spec. Pub., pp. 313–345.

Takahasi, E., Nakajima, K., Wright, T.L., 1998. Origin of the Columbia River basalts: melting model of a heterogeneous plume head. Earth Planet. Sci. Lett. 162, 63–80.

Taylor, S.R., McLennan, S.M., 1985. The Continental Crust: Its Composition and Evolution. Blackwell, Oxford Press, pp. 1–312.

Wang, K.Y., Hao, J., Zhou, S.P., Wilde, S., Cawood, P., 1997. SHRIMP dating of single grain zircon and its constraints on the Wutai orogenic event. Chin. Sci. Bull. 42 (1), 1295–1298.

Wang, Y.J., Fan, W.M., Guo, F., Li, C.W., 2003a. Biotite $^{40}Ar/^{39}Ar$ geochronology of the deformational rocks from Zanhuang metamorphic domain in southern Taihang mountains and their tectonothermal overprinting. Acta Petrol. Sinica 19 (1), 131–140 (in Chinese with English abstract).

Wang, Y.J., Fan, W.M., Zhang, Y.H., Guo, F., 2003b. Structural evolution and $^{40}Ar/^{39}Ar$ dating of the Zanhuang metamorphic domain in North China Craton: constraints on Paleoproterozoic tectonothermal overprinting. Precamb. Res. 122 (1–4), 159–182.

Wei, G.J., Liang, X.R., Li, X.H., Liu, Y., 2002. Precise measurement of Sr isotopic compositions of liquid and solid base using (LP) MC-ICP-MS. Geochimica 31 (3), 295–305.

Wilde, S.A., Cawood, P., Wang, K.Y., Nemchin, A., 1997. The relationship and timing of granitoid evolution with respect to felsic volcanism in the Wutai Complex, North China Craton. Proceedings of the 30th IGC. Precamb. Geol. Metamorphic. Petrol. 17, 75–88.

Wilde, S.A., Cawood, P., Wang, K.Y., Nemchin, A., 1998. SHRIMP U–Pb zircon dating of granites and gneisses in the Taihangshan-Wutaishan area: implications for the timing of crustal growth in the North China Craton. Chin. Sci. Bull. 43, 144 (abstract).

Wilde, S.A., Zhao, G.C., Sun, M., 2002. Development of the North China Craton during the late Archean and its amalgamation along a major 1.8 Ga collision zone: including speculations on its position within a global Paleoproterozoic supercontinent. Gondwana Res. 5, 85–94.

Winchester, J.A., Floyd, P.A., 1977. Geochemical discrimination of different magma series and their differentiation products using immobile elements. Chem. Geol. 20, 325–343.

Wu, C.H., Zhang, C.T., 1998. Paleoproterozoic SW–NE collision model for the central North China Craton. Prog. Precamb. Res. 21, 28–50 (in Chinese).

Xu, Y.G., Chung, S.L., Jahn, B.M., Wu, G.Y., 2001. Petrologic and geochemical constraints on the petrogenesis of Permian-Triassic Emeishan flood basalts in southwestern China. Lithos 58, 145–168.

Zhai, M.G., 1999. The 1.8 Ga thermal event in the North China craton: a record of early upwelling mantle Plumes. In: Lee, B.J., Lee, S.K., Kim, J., (eds). Crustal evolution in Northeast Asian. Taejon, KIGMM 1–3.

Zhai, M.G., Bian, A.G., 2000. Ultracontinental collision at the end of Neoarchean and its breakup between end of Paleoproterozoic and Mesoproterozoic in North China craton. Science in China (series D) (Supplement), 129–131 (in Chinese).

Zhai, M.G., Guo, J.H., Liu, W.J., 2001. An exposed cross-section of early Precambrian continental lower crust in the North China Craton. Phys. Chem. Earth (Part A) 26 (9–10), 781–792.

Zhai, M.G., Liu, W.J., 2003. Paleoproterozoic tectonic history of the North China Craton: a review. Precamb. Res. 122, 183–199.

Zhang, J.S., Dirks, P.H., Passchier, C.W., 1994. Extension collapse and uplift in a polymetamorphic granulite terrain in the Archean and Paleoproterozoic of North China. Precamb. Res. 67, 37–57.

Zhao, G.C., 2001. Paleoproterozoic assembly of the North China Craton. Geol. Mag. 138 (1), 89–91.

Zhao, G.C., Cawood, P.A., Lu, L.Z., 1999. Petrology and P-T history of the Wutai amphibolites: implications for tectonic evolution of the Wutai Complex. China. Precamb. Res. 93, 181–199.

Zhao, G.C., Cawood, P.A., Wilde, S.A., Sun, M., Lu, L., 2000. Metamorphism of basement rocks in the central zone of the North China Craton: implications for Paleoproterozoic tectonic evolution. Precamb. Res. 103, 55–88.

Zhao, G.C., Wilde, S.A., Cawood, P.A., Sun, M., 2001. Archean blocks and their boundaries in the North China Craton: lithological, geochemical, structural and P-T path constraints and tectonic evolution. Precamb. Res. 107, 45–73.

Zhao, G.C., Wilde, S.A., Cawood, P.A., Sun, M., 2002a. SHRIMP U-Pb zircon ages of the Fuping complex: implications for late Archean to Paleoproterozoic accretion and assembly of the North China Craton. Am. J. Sci. 302, 191–226.

Zhao, T.P., Zhou, M.F., Zhai, M.G., Xia, B., 2002b. Paleoproterozoic rift-related volcanism of the Xiong'er Group, North China Craton: implications for the breakup of Columbia. Int'l. Geol. Rev. 44 (4), 336–351.

Zhao, Z.P., 1993. Precambrian Crustal Evolution of the Sinica-Korean Platform. Sciences Press, Beijing (in Chinese).

Zimmer, M., Kröner, A., Jochum, K.P., Reischmann, T., Todt, W., 1995. The Gabal Gerf complex: a Precambrian N-MORB ophiolite in the Nubian Shield, NE African. Chem. Geol. 123, 29–51.